



LUND UNIVERSITY
Faculty of Science

Development of Spectroscopic Measurements for Raman and Thomson Scattering Diagnostics — Applications in Combustion and Plasma

Miaoxin Gong

Thesis submitted for the degree of Master of Science
Project duration: 8 months

Supervised by Andreas Ehn and Christian Brackmann

Department of Physics
Division of Combustion Physics
May 2019

LU TP 19-mn
May 2019

**Development of Spectroscopic Measurements
for Raman and Thomson Scattering Diagnostics**
—Applications in Combustion and Plasma

Miaoxin Gong

Division of Combustion Physics,
Department of Physics, Lund University

Master thesis supervised by Andreas Ehn, Christian Brackmann

Abstract

This thesis work concerns methods for improved spectroscopy including stray-light suppression, dynamic range improvement and signal enhancement. These methods were applied in Raman and Thomson- scattering spectroscopy in combustion and plasma. First, the stray-light suppression method Periodic Shadowing (PS) is implemented in an experimental setup with a high-power high repetition rate laser system used for Raman measurements in premixed, laminar, flat flames. It is shown that the background is reduced by a factor of 10 or more. Weak spectral lines can be distinguished and therefore better molecular species identification, concentration and temperature evaluation were performed. Second, initial test for Thomson scattering measurements in a gas discharge plasma was carried out with the experimental setup. Third, the method of using a Digital Micro-mirror Device (DMD) is combined with the PS method to boost the dynamic range in spectroscopic imaging. A novel DMD-PS spectrometer was designed and built and shows significantly enhanced performance, improving the dynamic range by a factor of at least 50. Such a high-dynamic-range and stray-light-reduced spectrometer has potential to be implemented in future imaging spectroscopy.

Popular Description

Combustion is a commonly used physical phenomenon in our daily life, from cooking to driving, heating and manufacturing. Typically, combustion starts to happen when fuel is mixed with an oxidant (usually oxygen in the air) and reaches a critical temperature. The process usually contains a complicated sequence of chemical reactions and also gives out intensive heat and light. As an important scientific task, significant research effort has been focused on understanding the physical and chemical processes in combustion.

Plasma is one of the fundamental states of matter in which an ionized substance becomes highly electrically conductive. Lightning is an example in nature of a partially ionized plasma. Plasma can be artificially generated as well. When electric current flows through a gaseous medium, gas discharge occurs and plasma is generated. Measuring the parameters of such laboratory plasma, termed plasma diagnostics, helps researchers to understand the physical phenomena.

Optical spectroscopy has played a significant role in many research fields, including combustion and plasma diagnostics. The interaction between matter and light can provide considerable amount of useful information. Therefore, specific light sources, such as lasers, can be employed as a probe to study the object of interest. With the advent of laser techniques, it is possible to achieve in-situ and non-invasive investigations with high spatial and temporal resolution. Raman spectroscopy is a diagnostic method based on Raman scattering, which is an inelastic light matter interaction. When light interacts with molecules, an energy exchange will take place between a photon and a molecule and the photon will scatter off with a different energy. The energy change of the photon coming in and out is determined in accordance with the species, providing a specific fingerprint on the spectrum. Similar to Rayleigh scattering, Thomson scattering is an elastic scattering process when light is scattered by charged particles, A Thomson scattered spectrum is broadened and important information of the plasma can be extracted from it.

However, spectroscopy suffers from interferences called stray light. Stray light in an optical system can be described as light that deviates from the intended path and ends up in the wrong place. In spectrometers, stray photons will distort the characteristics of the measured spectrum. Therefore, stray light can be a notable problem in spectroscopy, in particular when the spectral component of the signal-of-interest is near another strong spectral peak. The elimination or correction of stray light is desired in spectroscopic experiments. Several solutions to this problem have been developed at the Division of Combustion Physics at Lund University. This thesis work aims to apply such methods in Raman- and Thomson scattering measurements and also to test and demonstrate the performance.

Contents

Abstract	i
Popular Description	ii
List of Acronyms and abbreviations	v
1 Introduction	1
1.1 Motivation	1
1.2 Outline and goal of this thesis	2
2 Theoretical Background	3
2.1 Raman Scattering	3
2.1.1 Concentration Measurements	6
2.1.2 Temperature Measurements	6
2.2 Thomson Scattering	7
2.3 Periodic Shadowing Method	7
2.4 High Dynamic Range imaging	11
3 Experimental Method and Results for Raman measurements	12
3.1 Equipment	12
3.1.1 Lasers	12
3.1.2 Multi-pass system	12
3.1.3 Ronchi grating and the PS fiber	13
3.2 Setups	14
3.3 Combustion measurements	17
3.4 Results	17
3.4.1 The performance of the PS method	18
3.4.2 Species identification	20
3.4.3 Concentration measurements	22
3.4.4 Temperature evaluation	24
4 Experimental Method and Results for the DMD-PS spectrometer	26
4.1 Digital Micro-mirror Device (DMD)	26
4.2 The Optical design for the DMD-PS spectrometer	26
4.2.1 Ray tracing simulation	27
4.2.2 Alignment of the spectrometer	27
4.3 Results	29
4.3.1 Image transfer performance	29
4.3.2 Spectral resolution	31
4.3.3 Single peak removal	32
4.3.4 Multiple peaks removal	33

5	Experimental Method for Thomson measurements in plasma	33
5.1	Setup	33
5.2	Plasma Measurements	34
5.3	Preparation measurement	35
6	Quantifying the imaging quality of PS	36
7	Conclusion	38
8	Outlook	38
9	Acknowledgement	39

List of Acronyms and abbreviations

PS Periodic Shadowing

DMD Digital Micro-mirror Device

ICCD Intensified Charge-Coupled Device

CCD Charge-Coupled Device

SNR Signal-to-Noise Ratio

MTF Modulation Transfer Function

1 Introduction

1.1 Motivation

Optical diagnostics using lasers have a wide range of applications in numerous research fields in science [1]. Various spectroscopic techniques are developed from the different forms of light-matter interactions in terms of scattering. Inelastic light-matter scattering in gas phase can provide information on quantitative species-specific concentrations as well as information on global parameters such as temperature and pressure [2, 3]. Raman scattering is one of these processes where the scattered radiation changes its frequency due to gain or loss of energy which corresponds to energy level separations in an atom or molecule. It is therefore an inelastic scattering. Laser Raman spectroscopy offers a number of benefits for combustion diagnostics. First, it only requires a single laser for diagnosing many of the species of interest. Second, unlike resonance techniques that require specific laser frequencies according to the target species, Raman spectroscopy can be operated at any laser wavelength [4]. Third, the scattering only occurs along the beam path of the laser meaning that spatially resolved information can be acquired [5]. Also, it is easy to obtain absolute calibration by comparing the scattered signal of the species of interest with that of nitrogen [2].

However, Raman scattering is known to render weak signals, compared to elastic Rayleigh scattered light for example. Therefore, great care must be taken to distinguish the Raman signal from the Rayleigh signal. On one hand, a pulsed laser which delivers high average power can be used to compensate for the inherent weakness of the signals. The pulsed laser also allows rejection of continuous background signals which are typically present in combustion and plasma. On the other hand, the large amount of laser photons adds a laser-induced background that originates from light that scatters within the spectrometer. Such background is called stray light [6]. Stray light in a spectrometer system can be described as light that deviates from the intended path and distort the spectral characteristics of the detected light [7]. For spectral analysis of signals that have small spectral shifts from the laser wavelength, stray light can be a notable problem. Several solutions for stray-light suppression in spectrometers have recently been developed at the division of Combustion Physics at Lund University [8, 9], including a method called Periodic Shadowing (PS).

While Raman scattering occurs between photons and molecules, where an energy exchange between the photon and the molecule occurs, Thomson scattering is an elastic scattering process between a free electron and a photon. The spectral shape of the scattering signal can be used to evaluate the electron temperature. Thomson scattering is a powerful technique for plasma diagnostics. Similar to Raman scattering, Thomson scattering suffers from weak signals and stray light. Therefore, it is important to use a spectrometer with high background rejection, i.e. stray-light suppression technique for Thomson and Raman signals. The first and second part of this project aims to implement a novel stray-light suppression in spectrometers for Raman and Thomson measurements.

Furthermore, the contrast between the weak Raman peaks and the strong laser peak

(and also the contrast between a strong vibrational Raman peak and weaker rotational peaks) induces the need for High Dynamic Range imaging. Therefore, a Digital Micro-mirror Device (DMD) can be employed in the spectrometer design, playing a role as a spatial light filter at the spectrum plane [9]. This approach can be incorporated together with PS to achieve a high dynamic range, stray light suppressed spectrometer system. The third part of this project aims at building such a novel DMD-PS spectrometer. Figure 1 is a schematic diagram of the main issues and the corresponding solutions addressed in this thesis.

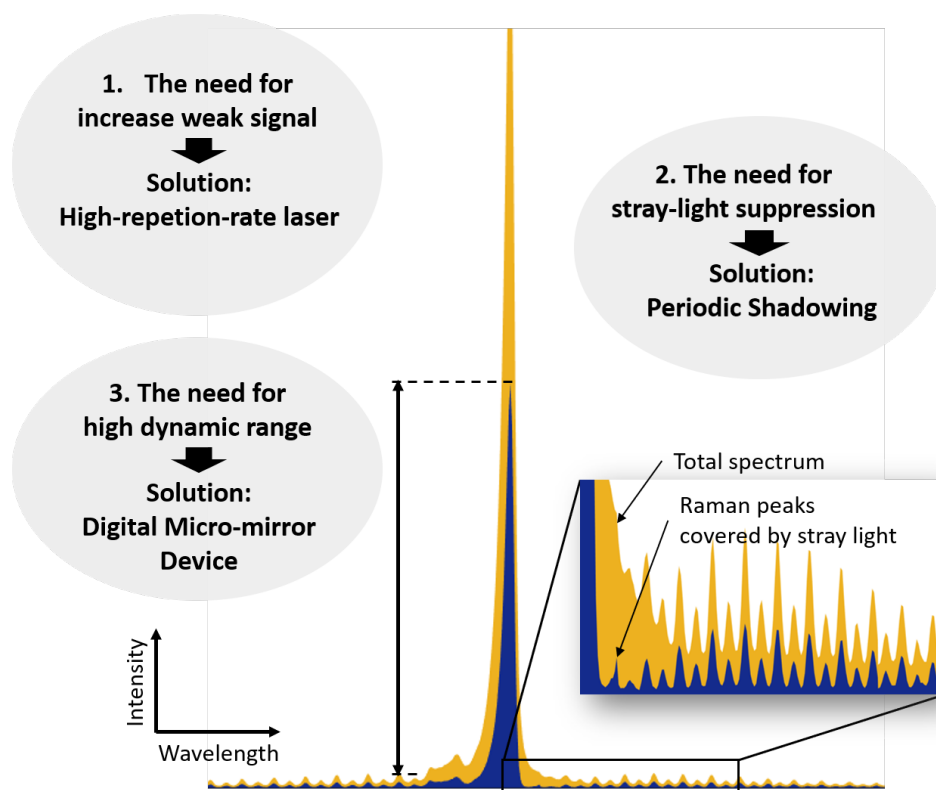


Figure 1: Schematic diagram illustrating the main issues and the solutions used in this thesis work. The spectrum is a typical vibrational Raman spectrum of nitrogen in air, where the yellow area is the total spectrum and the blue area is the Raman signal components interfering with stray light.

1.2 Outline and goal of this thesis

The aim of this project is to implement novel stray-light suppression methods into new experimental arrangements with high-power lasers for performing Raman- and Thomson scattering experiments in combustion and plasma diagnostics.

The project is divided into three parts. First, the stray-light suppression method Periodic Shadowing (PS) is implemented in the experimental setup and used for Raman mea-

measurements in laminar flames. Two different experimental approaches of the PS method are employed and tested, namely using Ronchi gratings [8] and specialized PS fibers [10] respectively and species identification, concentration measurement and temperature evaluation are performed. Second, an initial test to carry our Thomson scattering measurements in a gas discharge plasma is performed and the demands of the experimental arrangement are studied. However, at this point no Thomson scattered photons have been captured. Third, a novel spectrometer equipped with both DMD and PS is built in order to test the performance on suppressing certain spectral peaks, namely the strong laser peak present in Raman and Thomson scattering measurements.

2 Theoretical Background

2.1 Raman Scattering

The Raman scattering effect was first observed by C.V. Raman in 1928 and has been an important tool in many applications. The invention of the laser in 1960s boosted the application of Raman scattering as an analytical diagnostic method, including in the field of combustion diagnostics. Here the theory of Raman scattering restricted to the gas phase will be briefly introduced.

Photon scattering processes occur when photons interact with molecules. If the scattered photon carries the same energy as the incident photon (i.e. there is no energy exchange between the incident photon and the molecule), it is an elastic scattering process referred to as Rayleigh scattering. When there is energy transfer between the incident photon and the molecule, the inelastic scattering called Raman scattering occurs and it is termed vibrational, rotational or electronic depending on the type of the energy exchange [2]. Raman scattering can be described both by a classical approach and a quantum approach. In the classical sense, the Raman effect arises from the induced oscillating molecular dipole moment when the molecule is distorted by the electric field of the incoming light [2]. The molecule is said to be polarized and the dipole moment induced per unit electric field is termed the molecular polarizability, α . The induced dipole moment, \vec{p} , can be expressed as

$$\vec{p} = \alpha \vec{E} \quad (2.1)$$

where \vec{E} is the applied electric field from the incoming light and is depending on the frequency ν and the amplitude E_0 of the light wave. The polarizability changes periodically due to the fact that the molecule has vibrational and rotational motions, so the induced dipole moment for a vibrating molecule can be expressed as

$$\begin{aligned} \vec{p} &= (\alpha_0 + \beta_0 \sin 2\pi\nu_v t) E_0 \sin 2\pi\nu t \\ &= \alpha_0 E_0 \sin 2\pi\nu t + \frac{1}{2} \beta_0 E_0 [\cos 2\pi(\nu - \nu_v) - \cos 2\pi(\nu + \nu_v)] \end{aligned} \quad (2.2)$$

where α_0 denotes the value of polarizability at the equilibrium position of the molecule, β_0 is the amplitude of the change in the polarizability during vibration and ν_v is the vibrational frequency. The first term of equation 2.2 indicates the scattered light with the same frequency ν as the incident light and only changes the travelling direction of the photon without changing the energy, the Rayleigh scattering. The second term represents the Raman scattering process where the scattered light has shifted sidebands at frequencies $\nu \pm \nu_v$. This classical description of the Raman scattering gives a qualitative overall picture of the effect. For further quantitative predictions, a quantum mechanical treatment is needed for the scattering process [2].

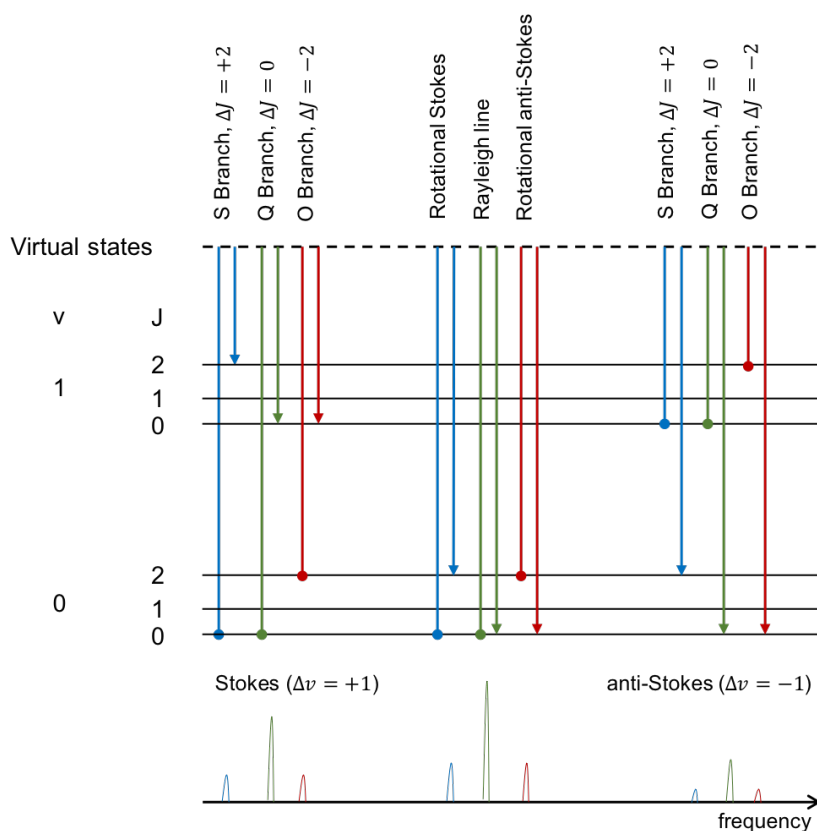


Figure 2: A simplified schematic energy level diagram of the Raman effect.

In the quantum mechanical sense, the incident laser light of frequency ν has photons of energy $h\nu$, where h is Planck's constant. After interacting with the molecules, the photons gain or lose energy according to the energy of the rotational or vibrational modes. In principle, Raman scattering occurs when $h\nu$ exceeds the energy difference between the states involved in the corresponding Raman transitions. As shown in the schematic energy level diagram in figure 2, the molecules are first excited to the virtual states and then immediately return to the final states. The emitted photons have energy that is equal to incident photon energy plus or minus the difference between the initial state and the

final state, and thus form a Raman spectrum. The spectral components where the incident photons gain energy are termed anti-Stokes components, while the ones that lose energy are called Stokes components. Quantum mechanical selection rules apply to Raman scattering since it involves transitions between quantum energy levels. For a linear molecule, the selection rule for rotational Raman scattering is $\Delta J = 0, \pm 2$, whereas for vibrational Raman scattering it is $\Delta v = 0, \pm 1$. The Raman spectral positions are thus predictable from the rotational and vibrational energies of a linear molecule. Firstly, we consider a pure rotational Raman spectrum when the rotational energy of state J can be written as (with the rigid rotor approximation)

$$F(J) = BJ(J + 1) \quad (2.3)$$

with $B = \frac{h}{8\pi^2 cI}$, where I is the moment of inertia of the molecule. The rotational lines of Stokes ($\Delta J = +2$) and anti-Stokes ($\Delta J = -2$) transitions occur respectively at frequencies

$$\nu_{Stokes} = \nu - 4B\left(J + \frac{3}{2}\right) \quad (2.4)$$

$$\nu_{anti-Stokes} = \nu + 4B\left(J + \frac{3}{2}\right) \quad (2.5)$$

where $4B$ is the distance between the equidistant Raman lines. The number of molecules N_J in the initial state is temperature dependent and given by the Boltzmann distribution

$$N_J = \frac{N}{Q_R} (2J + 1) e^{-BJ(J+1)hc/kT} \quad (2.6)$$

where N is the total number of molecules, Q_R is the function of the rotational partition and kT is the Boltzmann's constant times the temperature. In a similar manner, the vibrational transitions appears at $\nu \pm \nu_R$ and there are 3 branches, O, Q and S- branch corresponding to $\Delta J = -2, 0, +2$. As shown in figure 2, the intensity of the Q branch transitions is significantly stronger than the O and S branch- transitions. The vibrational-rotational Raman lines of the 3 branches have frequencies

$$\text{Q branch} \quad \nu_R = \Delta\nu_0 + (B_{v'} - B_{v''})J + (B_{v'} - B_{v''})J^2 \quad (2.7)$$

$$\text{S branch} \quad \nu_R = \Delta\nu_0 + 2B_v + (3B_{v'} - B_{v''})J + (B_{v'} - B_{v''})J^2 \quad (2.8)$$

$$\text{O branch} \quad \nu_R = \Delta\nu_0 + 6B_v + (5B_{v'} - B_{v''})J + (B_{v'} - B_{v''})J^2 \quad (2.9)$$

where $\Delta\nu_0$ is the vibrational frequency shift, $B_{v'}$ and $B_{v''}$ are the rotational constants of the initial and final state, respectively. The number of molecules in the vibrational state v can be given by

$$N_v = \frac{N}{Q_v} e^{-G_0(v)hc/kT} \quad (2.10)$$

where N is the total number of the molecules, G_0 is the vibrational energy of state v and Q_v is the vibrational partition function.

2.1.1 Concentration Measurements

From the intensity of the spectral peaks, it is possible to measure the concentration for the corresponding species from the Raman scattering. Due to the fact that the rotational Raman lines in gas mixtures usually are superimposed, it is common to use the vibrational Raman lines for concentration measurements. The intensity of a vibrational line is given by [11]

$$I = I_0 N l \sigma \Omega F(T) C \quad (2.11)$$

where I_0 is the incident laser intensity, N is the number density of the molecules, l is the sample volume extent, σ is the Raman cross section, and Ω is the solid angle of detection, $F(T)$ is a temperature dependent factor that is molecular specific, and C is a constant. The Raman cross section is in general determined experimentally. Table 1 shows some of the vibrational Q branch Raman cross sections at room temperature for the major species of interest in combustion [2].

Table 1: Raman cross sections for some molecules of interest in combustion studies [2] (unit of 10^{-30} cm²/sr).

Species	Vibrational frequency (cm ⁻¹)	Vibrational cross sections (532 nm)
N ₂	2330.7	0.37(Q)
H ₂	4160.2	0.943
O ₂	1556	0.47(Q)
CO	2145	0.48
CO ₂	1388 (ν_1)	0.6
	1285 ($2\nu_2$)	0.45
H ₂ O	3657	0.9
CH ₄	2915 (ν_1)	2.6
	3017 (ν_2)	1.7
C ₂ H ₆	3070 (ν_1)	3.7
	991 (ν_2)	5.6

The cross sections for spontaneous Raman scattering are very small, typically on the order of 10^{-30} cm² [11]. As a result, stray light from e.g. the strong laser and the strong vibrational peaks is usually an issue, since the weak rotational lines can be distorted and even concealed. Introducing an effective stray-light suppression method is therefore important in such measurements [8].

2.1.2 Temperature Measurements

Due to the fact that Raman scattering is temperature dependent, it is also possible to perform temperature measurements [2, 11]. The intensity of the Raman peaks is proportional to the Boltzmann factor, as shown in equations 2.6, 2.10 and 2.11. Both the rotational and

vibrational lines can be utilized for Raman thermometry. Rotational Raman thermometry will be demonstrated in the results section.

2.2 Thomson Scattering

In contrast to Rayleigh scattering where photons interact with molecules, Thomson scattering refers to the elastic scattering mechanism where photons collide with charged particles such as electrons and ions. Since the scattering effect of ions is usually small enough to neglect, Thomson scattering usually implies photon scattering with free electrons [5]. Thomson scattering is useful in plasma diagnostics as it can provide information on electron number density n_e and the electron energy distribution function (i.e. the electron temperature T_e) [12], as shown in figure 3. When the laser is injected into the plasma, the photons will be scattered. If the velocity distribution of electrons can be considered Maxwellian, the scattered power spectrum is Gaussian [13]. Due to the thermal motion of the electrons, the spectrum of the photons that are scattered off of electrons is Doppler broadened [5].

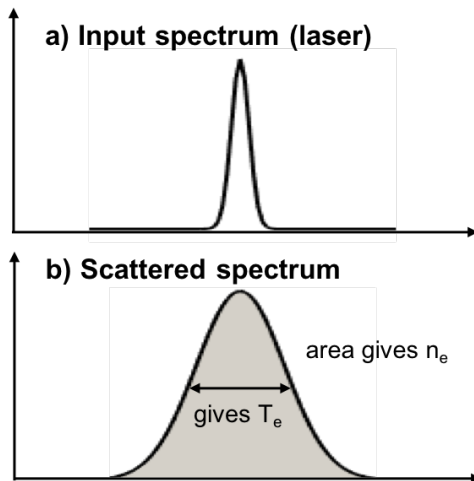


Figure 3: A schematic spectrum of Thomson scattering. The width of the broadened spectrum is proportional to $\sqrt{T_e}$ and the area of the peak is proportional to n_e .

2.3 Periodic Shadowing Method

Periodic Shadowing (PS) is a stray-light suppression method that is based on the idea of Structured Illumination Microscopy [14] and lock-in amplification [8]. Then signal photons are modulated with a predefined pattern when entering the spectrometer by either using a Ronchi grating or a specialized fiber. The approach by using a Ronchi grating is shown in figure 4 a). The Ronchi grating attached on the entrance slit of the spectrometer provides the spectral image a periodic shadow with a given spatial frequency and allows for further

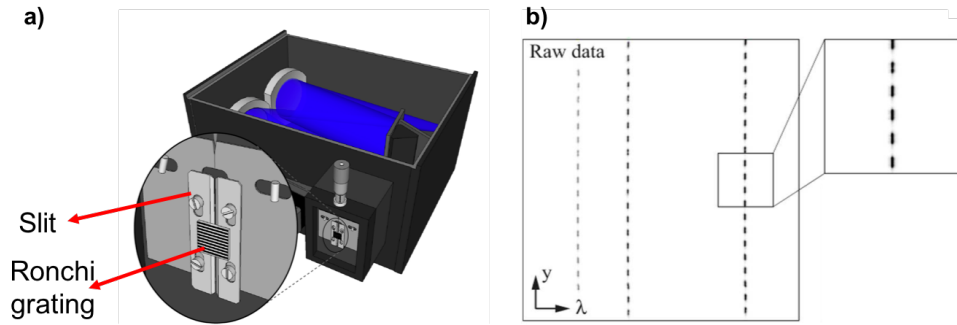


Figure 4: Illustration for an optical arrangement for Periodic Shadowing using a Ronchi grating. a) The Ronchi grating is tagged onto the entrance slit of the spectrometer. Image from [8]. b) The obtained 2D spectral image imposed with periodic shadow of an argon emission lamp is ready for PS post-processing.

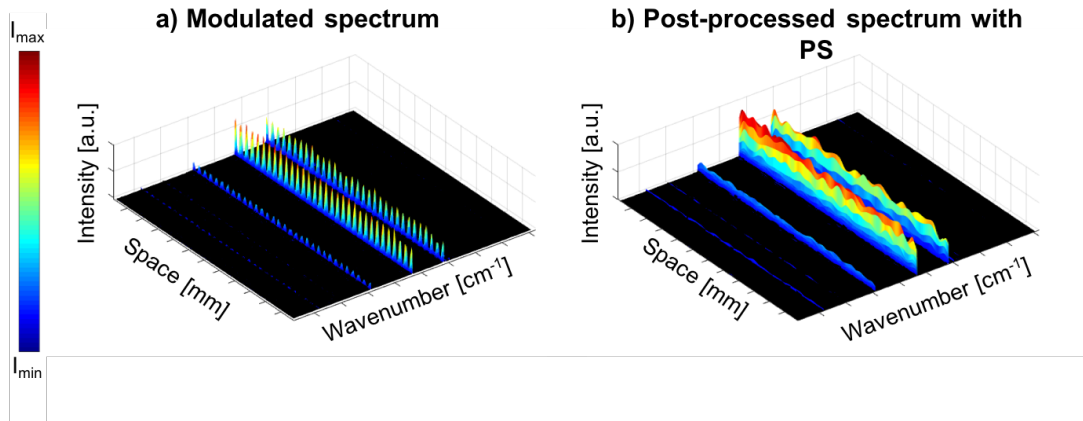


Figure 5: An example of PS data analysis. a) The unprocessed spectrum modulated along the vertical (spatial) direction. The spectrum is from a Raman measurement in air. b) The post-processed PS spectrum with stray-light removal.

post-processing, shown in figure 4 b). The stray light is scattered multiple times within the spectrometer and thus does not maintain the periodic pattern. In contrast, the signal light preserves the periodicity. Therefore, it is possible to distinguish and remove the stray-light component.

Figure 5 is an example of PS method. An intensity modulated spectral image of a Raman measurement in air is shown in figure 5 a). After Fourier transform column-by-column, each column is multiplied with two reference signals having a relative phase shift of 90 degrees. The modulated component is transformed into a DC component. Therefore, a band-pass filter can be applied to extract the signal information. The multiplication with the reference signals moves the stray light at low frequencies into higher frequencies so that it can be removed by the filter. Figure 5 b) shows the inverse Fourier transform of the filtered spectral image. A stray-light suppressed spectrum can be generated.

Lock-in amplifying allows for extracting a signal with a given carrier wave from a noisy environment [14]. This signal filtering method is often used for signals that are changing periodically over time. But it also works for signals with spatial modulation essentially. First, we consider a column in a modulated spectral image I , shown in figure 6, at wavelength λ that contains a spectral line:

$$I(\lambda, y) = A_\lambda(y) \sin(2\pi\nu_g y + \phi_\lambda(y)) + B_\lambda(y) \quad (2.12)$$

where y is spatial vector, ν_g is the modulation frequency of the Ronchi grating, A_λ is the amplitude of the modulated signal, B_λ is the amplitude of background with no modulation, and $\phi_\lambda(y)$ is the unknown spatial phase of the superimposed modulation. The lock-in process is to extract A_λ where the signal resides and reject B that contains background and stray light.

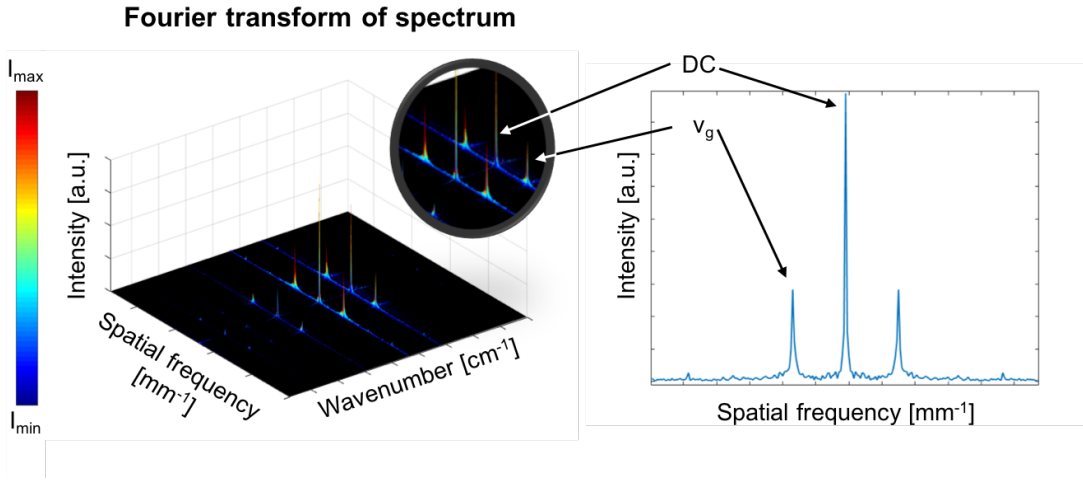


Figure 6: The figure on the left shows the Fourier transform of the spectral lines whereas the figure on the right shows the Fourier transform of a selected column in the zoomed in spectral line. The fundamental frequencies at $\pm\nu_g$ and the DC component are shown in the highlighted spectral line.

First, two reference signals I_{r_1} and I_{r_2} are formed by equations 2.13 and 2.14. These signals share the same periodicity ν_g with the modulated spectral lines and are 90 degrees shifted in phase.

$$I_{r_1} = \sin(2\pi\nu_g y) \quad (2.13)$$

$$I_{r_2} = \cos(2\pi\nu_g y) \quad (2.14)$$

Equations 2.15 and 2.16 are given by and simplified from multiplying the reference-signal vectors with the column vector $I(\lambda, y)$:

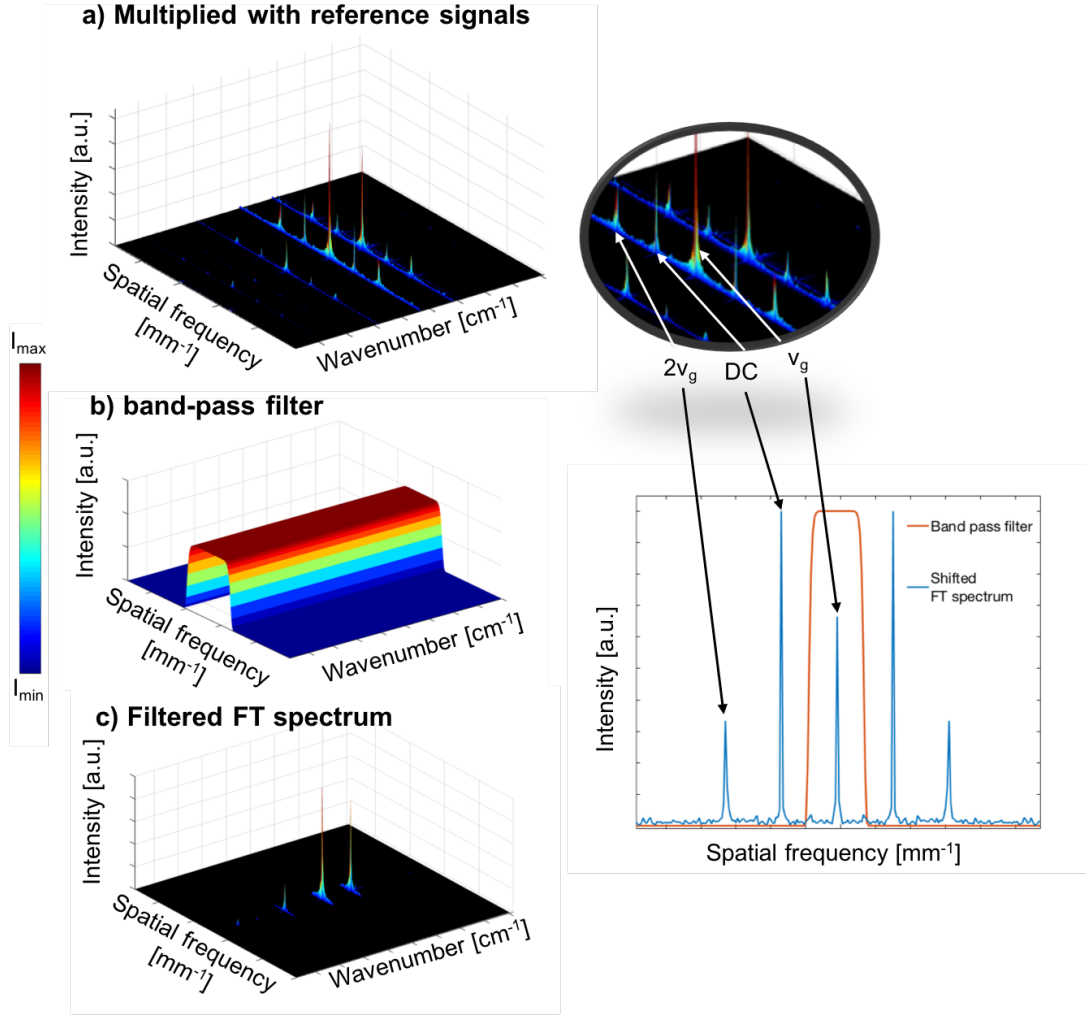


Figure 7: The steps of PS analysis. a) The Fourier transformed spectral lines are multiplied with a pair of reference signals, placing the fundamental peak at the origin while the DC component is moved to $\pm\nu_g$. b) The band-pass filter is then applied to the spectrum in order to extract the modulated information and filter out the high spatial frequency components. The selected column of the highlighted spectral line shows the shifting of the component and the shape of the filter. c) The resulting Fourier transform of the spectrum after filtering.

$$I_{\lambda}^1 = \frac{1}{2}A_{\lambda}(\cos(\phi_{\lambda}(y)) - \cos(4\pi\nu_g y + \phi_{\lambda}(y))) + B_{\lambda}\sin(2\pi\nu_g y) \quad (2.15)$$

$$I_{\lambda}^2 = \frac{1}{2}A_{\lambda}(\sin(\phi_{\lambda}(y)) + \sin(4\pi\nu_g y + \phi_{\lambda}(y))) + B_{\lambda}\cos(2\pi\nu_g y) \quad (2.16)$$

In this way, the DC component and the fundamental frequencies at $\pm\nu_g$ switch places,

as shown in 7 a). The modulated component is therefore transformed into a DC component so that when applying a band-pass filter with a cut-off frequency of $\nu_{cut} \leq \nu_g$ on equations 2.15 and 2.16, the DC component can be extracted.

$$\tilde{I}_\lambda^1 = \frac{1}{2} \tilde{A}_\lambda \cos(\phi_\lambda(y)) \quad (2.17)$$

$$\tilde{I}_\lambda^2 = \frac{1}{2} \tilde{A}_\lambda \sin(\phi_\lambda(y)) \quad (2.18)$$

where the tilde assignment indicates the applied frequency filtering. Extracted \tilde{A}_λ can be expressed as:

$$\tilde{A}_\lambda = 2\sqrt{(\tilde{I}_\lambda^1)^2 + (\tilde{I}_\lambda^2)^2} \quad (2.19)$$

2.4 High Dynamic Range imaging

In imaging spectroscopic measurements, it is a challenge to resolve weak and strong spectral peaks at the same time in the same frame and the the dynamic range of the imaging is drastically restrict. The present High Dynamic Range (HDR) imaging often refers to the method where several recordings of different exposure times are combined and merged into a single image [15, 16]. These recordings are adapted to capture the intense and dimmer regions respectively. In this way, the dynamic range can be improved considerably and this concept is used mostly for photography but also in spectroscopic imaging [17, 18]. However, there are several disadvantages with this approach. Because of the necessity of multiple exposures, the process is inherently slow and thus unsuitable for real-time measurements. Also, while capturing the dimmer regions with long exposure times, the saturation can result in permanent damage to the CCD chip. This effect is especially severe in spectroscopic measurements since the photon energy is concentrated along a small area on the CCD chip [9]. Furthermore, in measurements such as Raman and Thomson scattering, the stray light originated from the extreme strong spectral laser line also disturb the detection sensitivity. In order to overcome these issues, a novel spectrometer design equipped with a Digital micro-mirror Device and performing Periodic Shadowing was first reported by Kristensson et al. (2016) [19]. With this design, it is possible to improve the dynamic range in a single exposure and also reduce the interference from the stray light.

3 Experimental Method and Results for Raman measurements

3.1 Equipment

3.1.1 Lasers

In this project, two high-power high-repetition-rate pulsed laser systems were employed. In the first half of the experiment, a Litron LDY304 DPSS Laser was employed. This Dual Head Diode Pumped Q-switched Nd:YLF laser system has the wavelength at 527 nm and the maximum output pulse energy of 20 mJ and average power of 30 W at 1 kHz. The pulse duration is about 150 ns. In the second half of the experiment, a Edgewave HD40I-OE Nd:YAG laser was employed. The wavelength is 532 nm and the maximum output power is 100 W. The Nd:YAG laser was controlled by a BNC M575 external pulse generator, providing pulses at a frequency of 5 kHz and a pulse duration of 75 μ s, in combination with use of gated detection by the high-speed ICCD camera. The short camera gate reduces the background level significantly.

3.1.2 Multi-pass system

To improve the utility of the laser beam, a multi-pass system was designed and employed. The multi-pass setup contained a lens and a pair of concave mirrors. The lens was located before a hole on the first concave mirror, leading the light through the hole and focusing the laser beam at the center of the mirror cavity located above the burner surface. Multi-pass beam paths were generated within the cavity, forming a focal probe volume at the center where 32 beam paths pass through both back and forth.

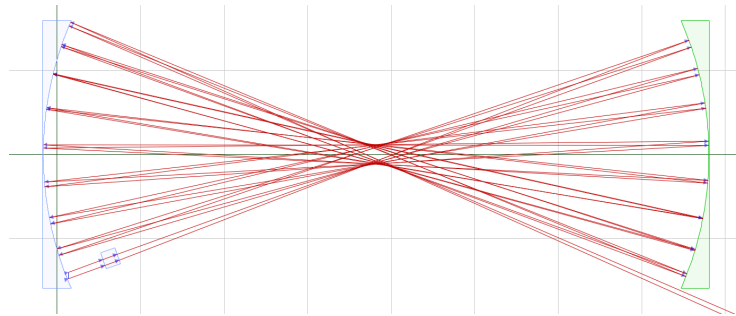


Figure 8: Schematic illustration of the multi-pass beam paths in simulation. (made by Haisol Kim)

A Ray tracing simulation of the multi-pass arrangement is shown in figure 8. In order to achieve high spatial resolution in the vertical direction, the beam pattern was adjusted to propagate on the same level as much as possible [20]. The probe volume therefore can be approximately considered as a horizontal laser sheet with about 0.5 mm height and 5×2 mm size.

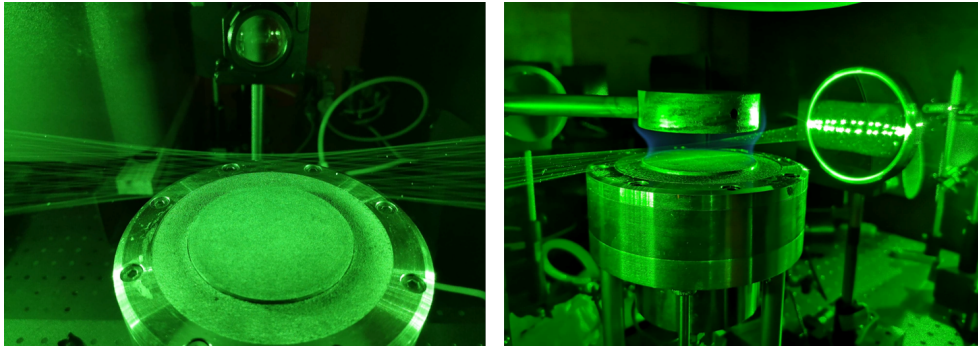


Figure 9: Photographs from different views of the multi-pass beam paths. (credit to Jim Larsson)

3.1.3 Ronchi grating and the PS fiber

For the PS method, as mentioned in section 2.3, there are two approaches to create the periodic modulation of the incoming light. The first and most common way is by using a Ronchi grating. A Ronchi grating is an optical mask which consist constant-interval bar. As mentioned in 2.3, inserting the Ronchi grating on the entrance slit of the spectrometer will effectively create the periodic stripe pattern with a given spatial frequency. Ronchi gratings with 2 1/mm and 5 1/mm were used in the experiment.

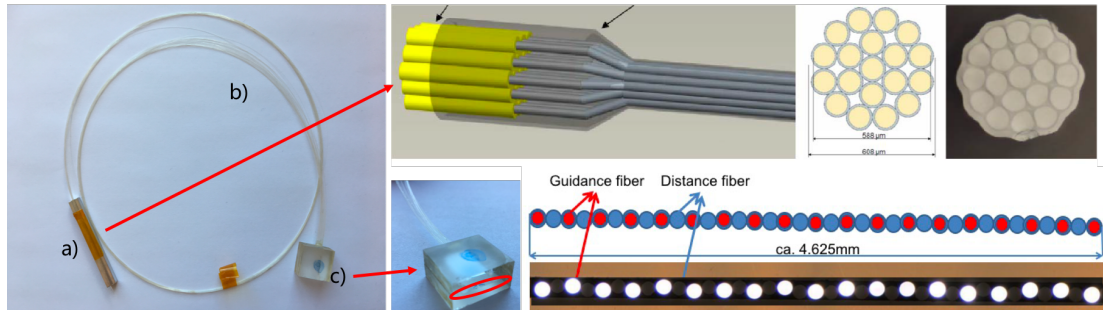
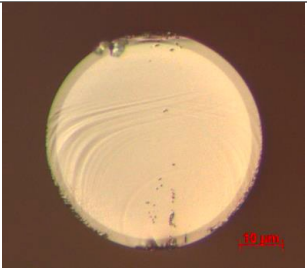
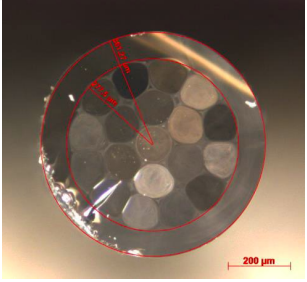
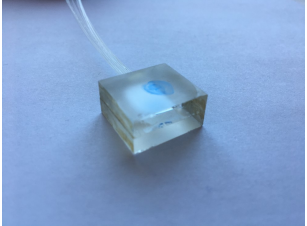


Figure 10: Illustration of the specialized PS fiber. a) The input end of the fiber bundle fixed in a capillary with circular layout contains 19 individual fibers. b) The length of the fibers is about 0.5-1.0 m. c) The output end of the fibers is arranged in linear layout. Every two fibers from the input end are interspersed by a distant fiber which is identical to them.

An alternative is to use a specialized fiber manufactured for the PS method [10], as shown in figure 10. This 'PS fiber' features that it can transport and modulate the light at the same time. The fiber is made of 19 individual and identical multi-mode fibers. The fiber bundle is arranged into a circular structure at one end (the input end) and a linear structure on the other end (the output end). Each active fiber (guidance fiber) at the output end is separated by an identical 'dead' fiber (distance fiber) so that a unique

pattern with a fixed spatial frequency is created when light is inserted into the input end. Compared with the Ronchi grating where 50% of the incoming light is rejected, the use of the fiber prevents light loss and brings flexibility to the optical arrangement in principle.

Table 2: General dimensions of the PS fibers (measured by the manufacturing group)

	Approximate dimensions	Photograph
Fiber	Fiber core diameter: 114 μm ; Cladding diameter: 126 μm ; Coating diameter: 230 μm	
Capillary for input end	Outer diameter: $\sim 1610 \mu\text{m}$ Inner diameter: $\sim 1294 \mu\text{m}$	
Glass holder for output end	LWH: $2.0 \times 1.0 \times 0.5 \text{ cm}$	

3.2 Setups

The two experimental setups for the Raman measurements are shown in figure 11 and 12. Figure 13 is a photo of the experimental setup during operation, where severe scattering of laser light can be observed. Figure 11 is the schematic illustration of the setup where a Ronchi grating is attached at the entrance slit of the spectrometer to create the spatial modulation for PS method.

The laser beam was generated and led by mirrors M1 and M2 towards M3. M3 was a pair of plane mirrors to change the polarization direction and the height of the laser beam. The laser beam was then focused by lens L1 at the center of the cavity and passes through apertures PH1 and PH2. A pair of dichroic Multi-pass mirrors was placed to guide the laser beam and formed the multi-pass pattern. With fine adjustment of the vertical and horizontal position of the optics, the multi-pass laser pattern was focused at the center above the burner. The burner was placed on a vertical translation stage so that different

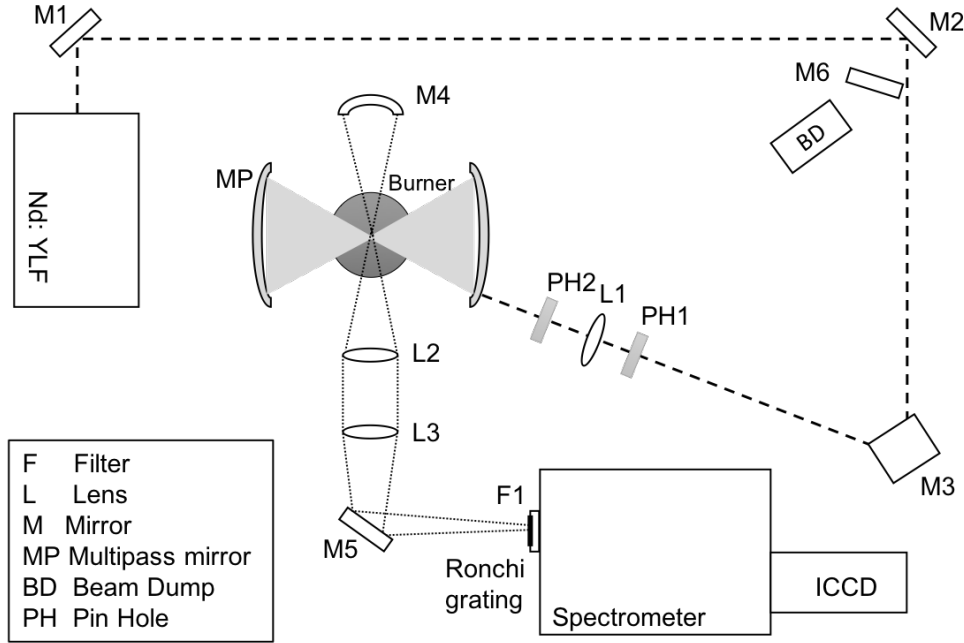


Figure 11: Schematic illustration of the experimental setup for Raman scattering measurements using the Ronchi grating for PS modulation.

heights (min scale of about 0.1 mm) of the flame can be measured. The back reflected laser beam was directed by mirror M6 into the beam dump BD. In order to capture additional Raman signal, a spherical mirror M4 was placed behind the burner. The Raman signal was collected and focused by lens L2 and L3 and then reflected by mirror M5 onto the entrance slit of the spectrometer. A Semrock EdgeBasic BLP01-532R-25 long-pass filter was placed in front of the slit to filter out the strong scattered light from the laser.

The Princeton Instruments IsoPlane SCT-320 grating spectrometer with a rotational grating stage was employed. A grating of a groove density 1800 l/mm blazed at 500 nm and another grating of a groove density 2400 l/mm blazed at UV are used in the measurements. The entrance slit was manually controlled and set to $50 \mu\text{m}$ width to obtain high spectral resolution. The Princeton Instruments PI-MAX4 ICCD camera (chip size 1024×256 pixels) was mounted at the output of the spectrometer. The camera was triggered by the laser to synchronize with the pulses with a short gate width so that the continuous background can be suppressed. One exposure per frame was used, while the on-CCD accumulation and intensifier gain were adjusted for different conditions during the measurements.

Figure 12 is the schematic illustration where the PS fiber is used to collect and create the PS modulation for the Raman measurements, replacing the Ronchi grating. The Raman signal was focused onto the input end of the PS fiber instead of directly onto the entrance slit of the spectrometer. Then the signal transmitted through the fiber bundle and reached the entrance slit with the PS pattern formed. The output end of the PS fiber was placed on a level plate to fine adjust the relative position in relation to the slit. Note that the size

of the focused image from the probe volume is larger than the size of the input end of the PS fiber and the size of the output end is also larger than the slit width. This issue leads to inevitable signal loss, which reduces the signal strength considerably.

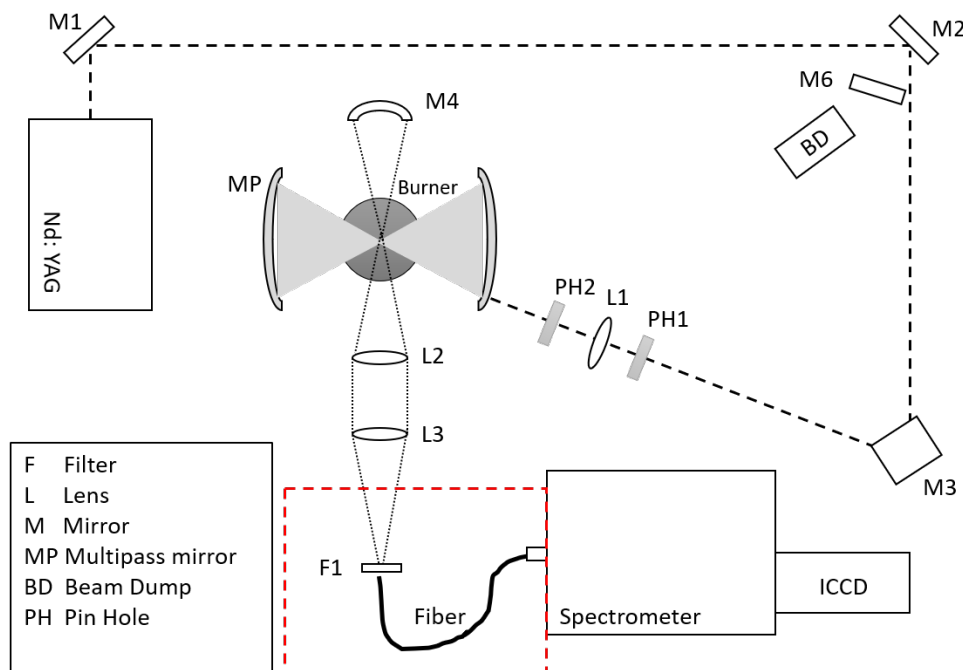


Figure 12: Schematic illustration of the experimental setup for Raman scattering measurements using the PS fiber for signal collection and PS modulation.

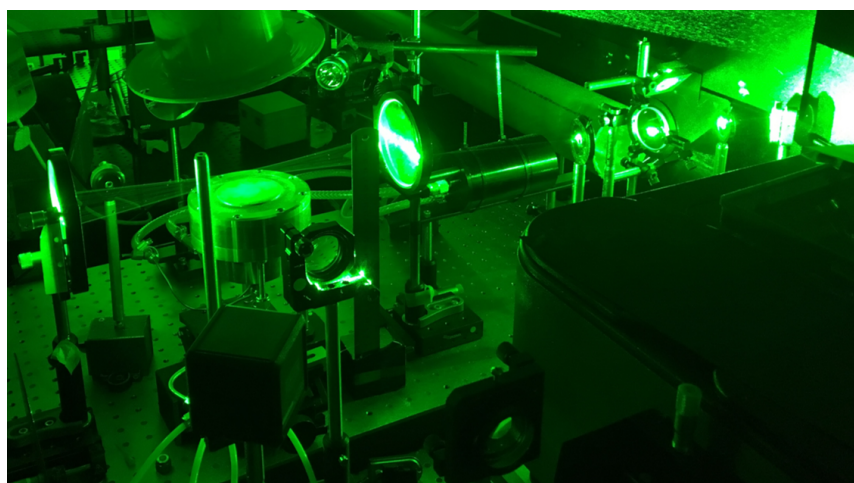


Figure 13: Photograph of the Raman setup during operation.

3.3 Combustion measurements

The initial measurements were carried out on oxygen and nitrogen in ambient air. A porous plug flat flame (McKenna) burner, burning premixed hydrocarbon gas/air mixtures, was used in Raman combustion measurements. The flow rates were controlled by a set of gas flow controllers. All the flames listed below were operated at atmospheric pressure. Figure 14 shows a methane/air flame (equivalence ratio $\phi = 1.0$) burning and how the laser beam paths travel through the flame in a plane.

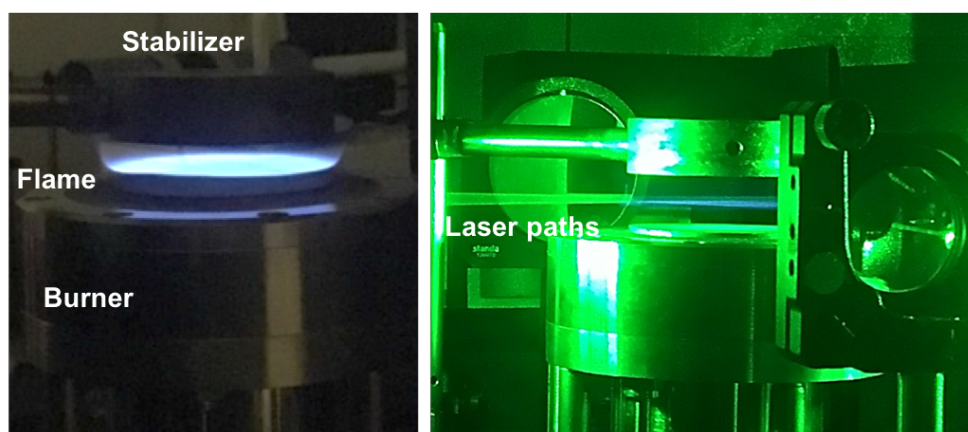


Figure 14: Photos of premixed flat methane/air flame of $\phi = 1.0$.

Methane, ethane, hydrogen/air premixed flame Methane (18%), ethane (72%), hydrogen (10%)/air premixed flames of three different equivalence ratio $\phi = 0.8, 1.0, 1.2$ were used in the first part of the measurements. An additional nitrogen flow was used to lift the flame above the burner surface. Each flame was scanned through height above burner in steps of about 0.2 mm from the unburned reactant zone to the combustion product zone respectively.

Methane/air premixed flame A methane/air premixed flame of $\phi = 1.0$ was measured at four heights above burner (3.0 mm, 7.0 mm, 9.0 mm, 12.0 mm).

3.4 Results

During the measurements, the accumulation time was adjusted to the signal strength in each case and the intensifier gain was kept the same in each case so that the spectrum intensity can have a linear relation to the acquisition time. All the spectra were normalised by unit acquisition time to enable comparisons. The wavelength was calibrated by a calibration lamp. Intensity calibration was carried out by using a broadband lamp with know spectral profile.

3.4.1 The performance of the PS method

The capabilities and performance of the PS technique in Raman measurements were verified and demonstrated experimentally in the reactant zone and the product zone (i.e. room temperature and high temperature condition) of the $\phi = 1.2$ methane, ethane, hydrogen/air premixed flame, shown in figure 15 and 16.

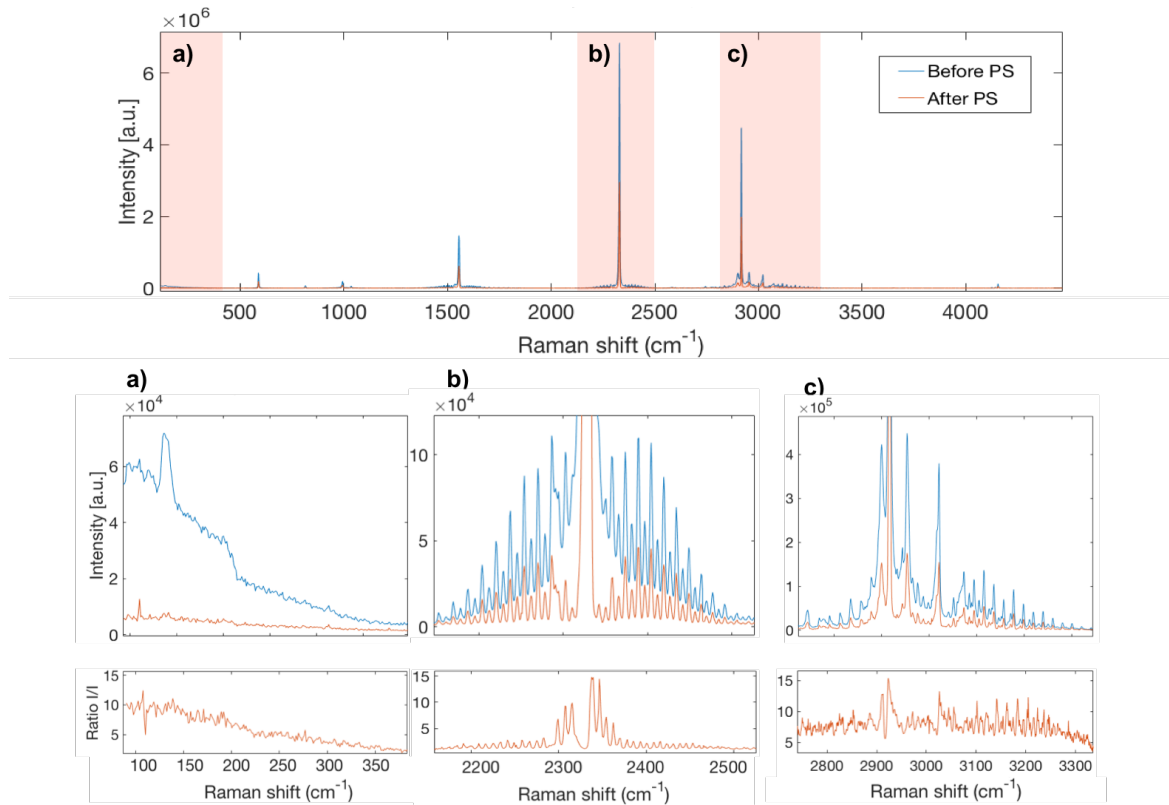


Figure 15: Raman spectra of the reactant zone ($h=5.3$ mm) of the premixed methane, ethane, hydrogen/air flame, before and after PS process. a), b), c) show the zoomed-in spectra and the ratio between spectra before and after PS filtering at three informative regions.

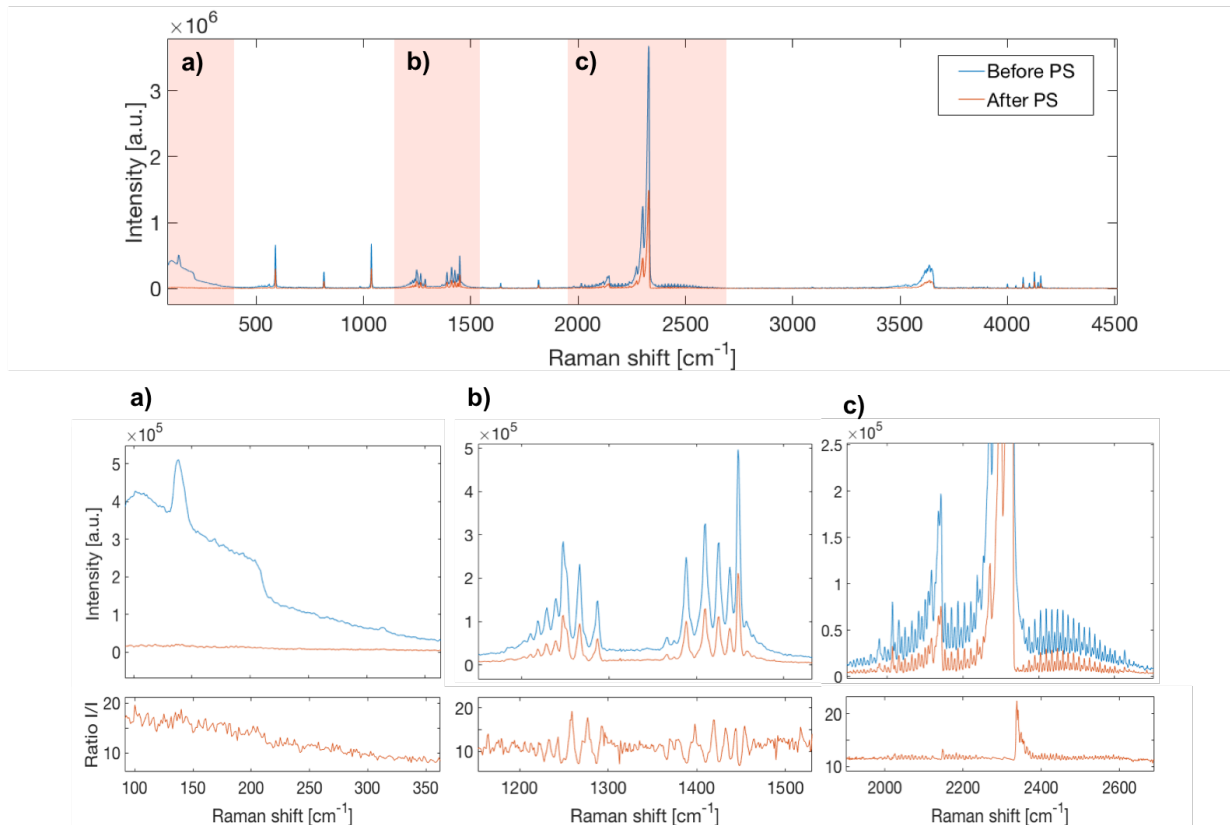


Figure 16: Raman spectra of the product zone ($h=12.5$ mm) of the premixed methane, ethane, hydrogen/air flame, before and after PS processing. a), b), c) show zoomed-in spectra and the ratio between spectra before and after PS filtering at three informative regions.

Note that the 527 nm laser was used in this measurement so the low Raman shift wavenumber rotational signals were filtered out by the 532 nm long-pass filter. Figure 15 shows the spectra of the reactant zone of the $\phi = 1.2$ methane, ethane, hydrogen/air premixed flame, a), b), c) show spectra from three regions and their corresponding ratio between the spectrum before PS and after PS. At the low Raman shift wavenumber region, the laser-induced background level is higher than other spectral regions because of the stray light production from the elastic scattering processes. Figure 15 a) demonstrates that the stray light is effectively reduced by PS in the low Raman shift wavenumber region, by a factor of about 10. Figure 15 b) shows the rotational lines of the O and S branches of N_2 . The first rotational lines aside the strong vibrational Q branch peak are clear to see in the spectrum after PS, while they are not visible in the spectrum before PS due to stray light from the strong Q branch. This suggests that the PS method is able to reveal weak peaks that are hidden by stray light. In addition, the envelope shape of the rotational band is restored after PS, which may allow for thermometry in Raman experiments. The spectrum of figure 15 c) displays the hydrocarbon region. This shows that the PS method is also applicable for analysis of combined and/or overlapping spectral lines.

Figure 16 shows spectra of the product zone, where the temperature is higher. As shown in 16 a), the PS method works for high temperature condition in the low-wavenumber region as well. Compared with the room temperature case, the stray light level has increased. It may arise from the increased scattering processes when the laser is closer to a burner surface. The stabilizer is placed closer to the laser focus when measuring the high-temperature area and more light scatters from the surface. Figure 16 b) shows the peaks of the combustion product CO_2 . The stray light component is removed without changing the spectral information of the spectral peaks. Figure 16 c) shows the N_2 vibrational and rotational peaks. At high temperature, the molecule starts to be populated in the excited states of $v = 1, v = 2$ and gives rise to a spectrum of these characteristic shaped bands because of the molecular anharmonicity. The “hot band” from $v = 1 \rightarrow v = 2$ appears in addition to the fundamental band $v = 0 \rightarrow v = 1$. These bands have a separation of only about 30 cm^{-1} and it is well-resolved in the PS spectrum. Similarly to the observation at the low-temperature condition, the spectrum after PS resolves more rotational peaks.

These demonstrations indicate that the PS method is an effective tool for stray-light suppression for Raman measurements, especially in regions where weak spectral lines are close to a strong one. Moreover, the original spectral structure still remains after the process. It is also beneficial for combined spectra as the Raman measurements are often applied to multi-species diagnostics. Similar measurements are also made using the PS fiber and it also shows good performance on stray-light reduction.

3.4.2 Species identification

Many species of interest in combustion can be measured in the same spectrum with Raman spectroscopy. As the McKenna burner provides steady, flat, laminar premixed flames, it is possible to use long acquisition times during the measurements and therefore improve the detection sensitivity and accuracy. Also, high spatial resolution was achieved by combining with the high power pulsed laser in the multi-pass arrangement. By scanning the flame through heights, the chemical compositions at different reaction stages in the combustion process can be studied.

Figure 17 shows PS spectra of the $\phi = 1.2$ methane, ethane, hydrogen/air premixed flame at three heights representing unburned zone, reaction zone and product zone respectively. These spectra are selected from 13 spectra measured at different height with a step of about 0.2 mm, by changing the height of the burner on the translation stage. Figure 17 a) shows the hydrocarbons decrease gradually as the combustion reaction processes. Figure 17 b) shows the region of O_2 and CO_2 . The hot band of the O_2 vibrational peak starts to appear in the reaction zone as the temperature increases. In product zone, the O_2 peak is almost extinct for the equivalence ratio is $\phi = 1.2$ so the O_2 is consumed completely. As for the CO_2 , significant growth can be observed. Also, the hot band of CO_2 shows up in the high temperature product zone. In figure 17 c), the distribution of the N_2 vibrational peak is clearly transformed as the temperature changes. Although N_2 essentially does not react in the combustion process, the signal strength is reduced because the number density is reduced when the temperature increases. CO increases during the

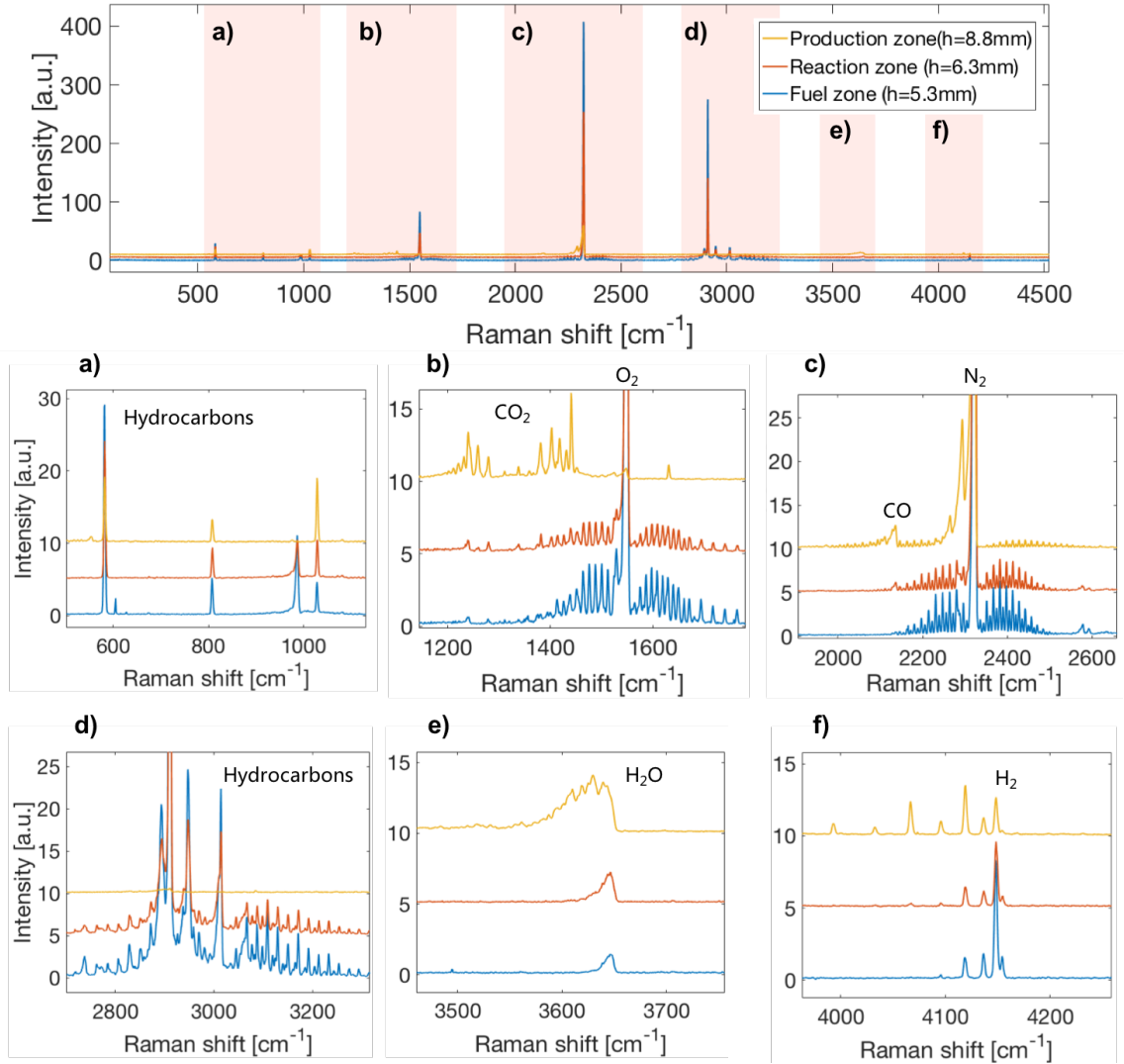


Figure 17: The PS spectra of the $\phi = 1.2$ methane, ethane, hydrogen/air premixed flame at three heights of fuel zone ($h=5.3$ mm), reaction zone ($h=6.3$ mm) and product zone ($h=8.8$ mm) respectively. a), b), c), d), e), f) show the zoomed-in spectra of the major species of interest.

combustion process as it is one of the products and appears at 2100 cm^{-1} . Figure 17 d) is the region where vibrational hydrocarbon lines are located. The trend is clear that the fuel is consumed after the combustion. There are also intermediate hydrocarbon radicals present in the reaction zone though it is difficult to identify and distinguish them. Figure 17 e) shows the spectrum of H_2O . The amount of H_2O has grown and the hot band starts to arise in the product zone. The structure of the H_2O spectrum is complex compared to diatomic molecules such as N_2 . Spectral synthesis needs to be considered when estimating concentration from the spectrum. Figure 17 f) displays the spectrum of H_2 . The intensity

decreases as the temperature increases and the hot band arises at the high-temperature condition.

3.4.3 Concentration measurements

The Raman spectra of the flames along the heights above burner allowed for concentration measurements of the major species. Here, the major species mole fraction profiles for the methane, ethane, hydrogen/air flame of three different equivalence ratio ($\phi = 0.8/1.0/1.2$) were calculated from the measured spectra and theoretically using Cantera [21] with Glarborg et al. (2018) mechanism [22]. The major species included: N_2 , O_2 , CH_4 , CO_2 , H_2O , CO , H_2 , assuming these gases constitute 100% of the total molecules in the flames. The mole fraction of each species was calculated by multiplying the spectral area and the corresponding Raman cross-section value divided by the total sum of these quantities. The Raman cross-sections and the corresponding Raman shift values are listed in table 1. Figures 18, 19 and 20 show the calculated mole fraction from the measurements (left) and the Cantera program (right) of $\phi = 0.8$, $\phi = 1.0$ and $\phi = 1.2$ respectively. Note that N_2 is present but not illustrated in the scales. It is shown that the experimental results and the theoretical calculations agree with each other to a large extent.

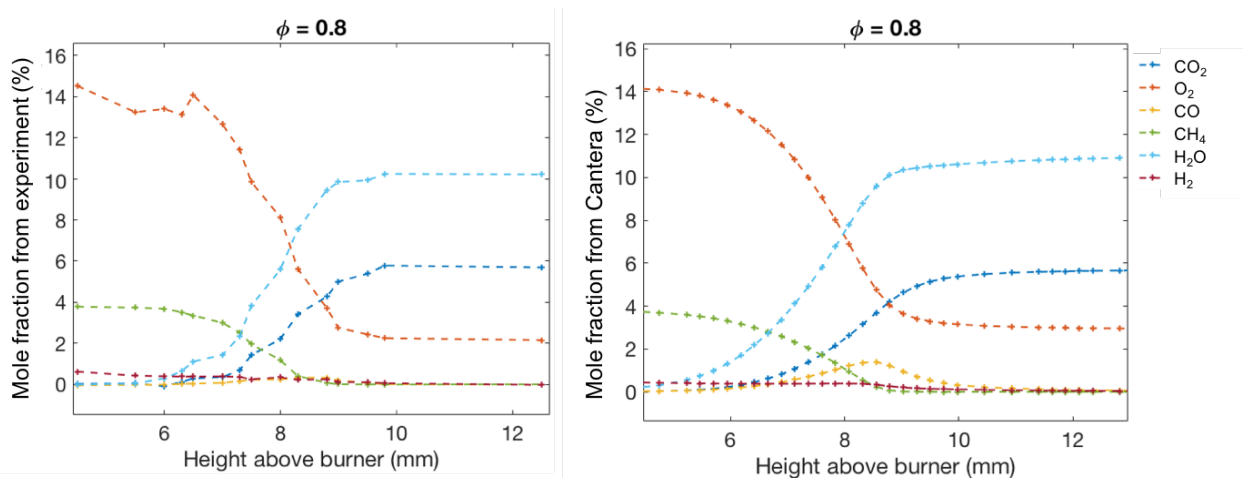


Figure 18: Mole fraction of major species from experiment (left) and Cantera calculation (right) in methane, ethane, hydrogen/air flame of $\phi = 0.8$.

The mole fraction profiles of the three flames with different equivalence ratios share several common features. First, the H_2O component appears to be lower than the theoretical calculated value. It may be due to the fact that the H_2O peak is a complex spectrum, as mentioned in 3.4.2, and directly calculate the spectral area from integral leads to underestimation on the component. Fitting to each peak may be required to obtain more accurate result. Second, the experimental curves appear less smooth than the theoretical prediction, especially at the gradients representing the reaction zone region. This may originate from fluctuations when the laser beam enters this region of the flame. Also, the

spectra are acquired through long averaging times so that the fluctuations are recorded in the data. This effect is more obvious in the rich flame ($\phi = 1.2$) case than the lean ($\phi = 0.8$) and stoichiometric flame ($\phi = 1.0$) cases.

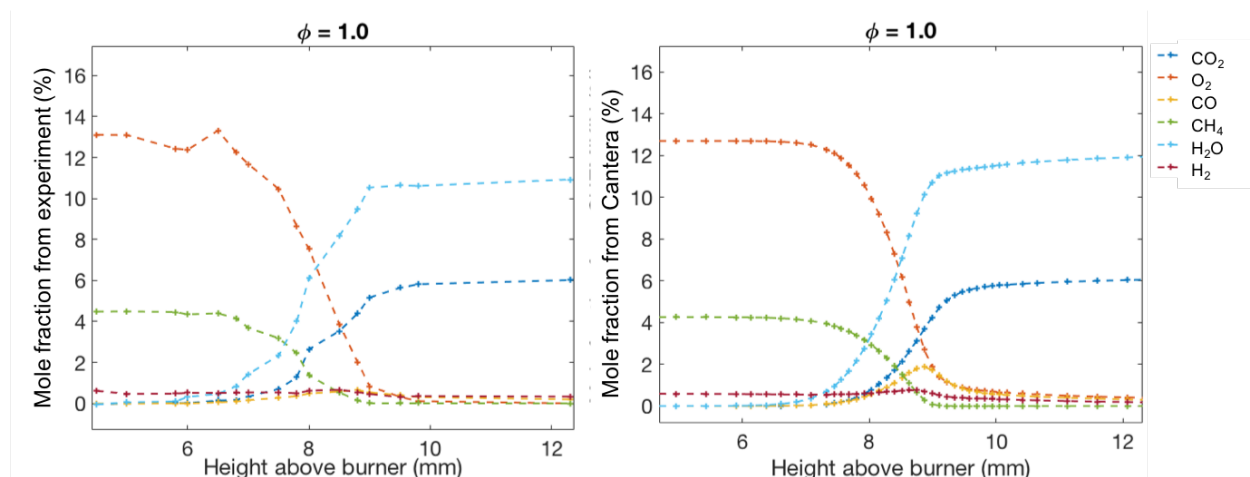


Figure 19: Mole fraction of major species from experiment (left) and Cantera calculation (right) in methane, ethane, hydrogen/air flame of $\phi = 1.0$.

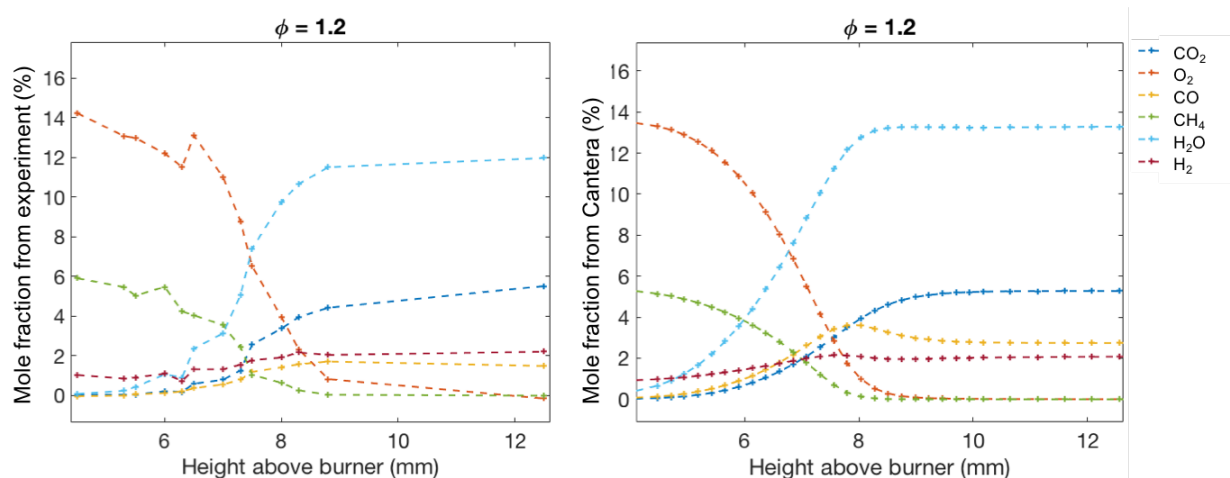


Figure 20: Mole fraction of major species from experiment (left) and Cantera calculation (right) in methane, ethane, hydrogen/air flame of $\phi = 1.2$.

Thirdly, the experimental CO curves do not contain the hump feature as it shows in the theoretical calculations. The reason may be that the CO lines overlap with the rotational lines of N_2 , as shown in figure 21. When the temperature increases, the molecule distribution changes and the part of rotational N_2 lines where overlaps with the CO lines increases. However, the CO concentration is fairly low compared to N_2 concentration. As a result, the trend of CO concentration that it increases first and then decreases as the

temperature increases cannot be seen when the rotational N_2 lines are added up with the CO lines. Subtraction of the rotational N_2 may be needed for better result.

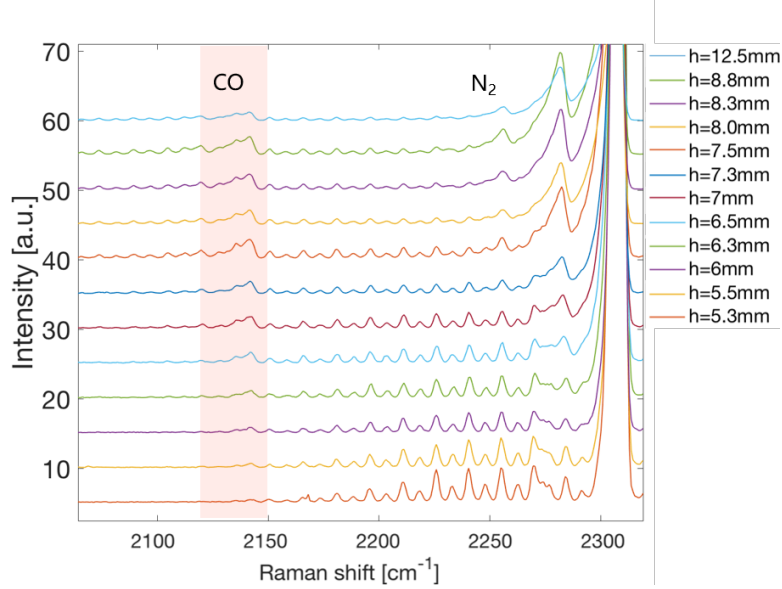


Figure 21: The zoomed-in PS spectra at CO and N_2 region of the $\phi = 1.2$ methane, ethane, hydrogen/air flame at different heights above burner. The rotational N_2 lines overlap with CO lines especially in the high temperature conditions, which may result in the inaccuracy of the CO concentration evaluations.

3.4.4 Temperature evaluation

Raman scattering is suited for temperature measurements since the envelope shape of the Raman lines follows the Boltzmann distribution. Here, a simple temperature estimation was performed by comparing the experimental spectra with theoretical simulations of pure rotational Raman lines of nitrogen. Rotational spectra measured at four different heights in a premixed methane/air flame ($\phi = 1.0$) were investigated. The theoretical simulation was performed by the PGOPHER program [23].

Figure 22 shows the PS spectra at the different heights in the methane/air premixed flame. The PS method is applied by using the PS fiber. The stray light level is extremely high at the low-wavenumber region. Nevertheless, the PS process effectively reduces the background level and largely restores the envelop shape of the rotational lines, allowing for comparison with the simulation spectra, as shown in figure 23.

Figure 23 shows the comparison between the experimental and the simulation spectra. Note that the intensity of each pair is sealed to the maximum intensity in order to be comparable. The experiments and the simulation show a good agreement. In the low temperature cases, the nitrogen lines are superimposed with the oxygen lines of air. In the high temperature cases, the oxygen is consumed while the stray light level increases.

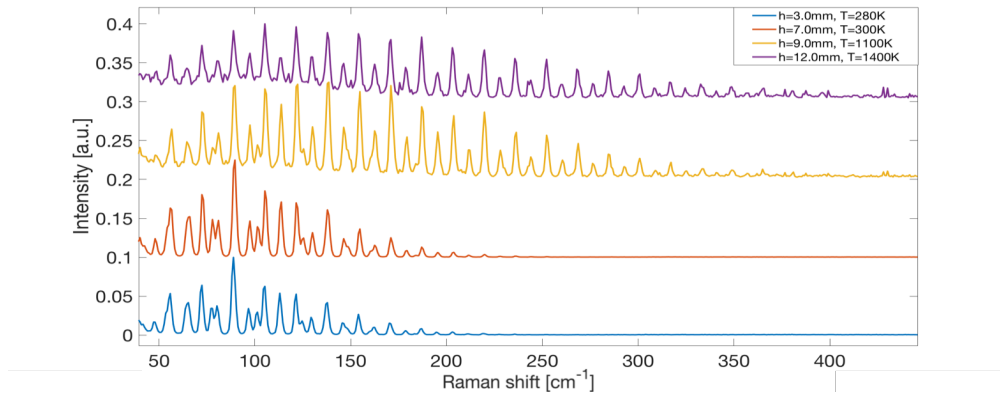


Figure 22: Rotational Raman PS spectra at different heights in the methane/air flame ($\phi = 1.0$). The temperature values are obtained by curve fitting.

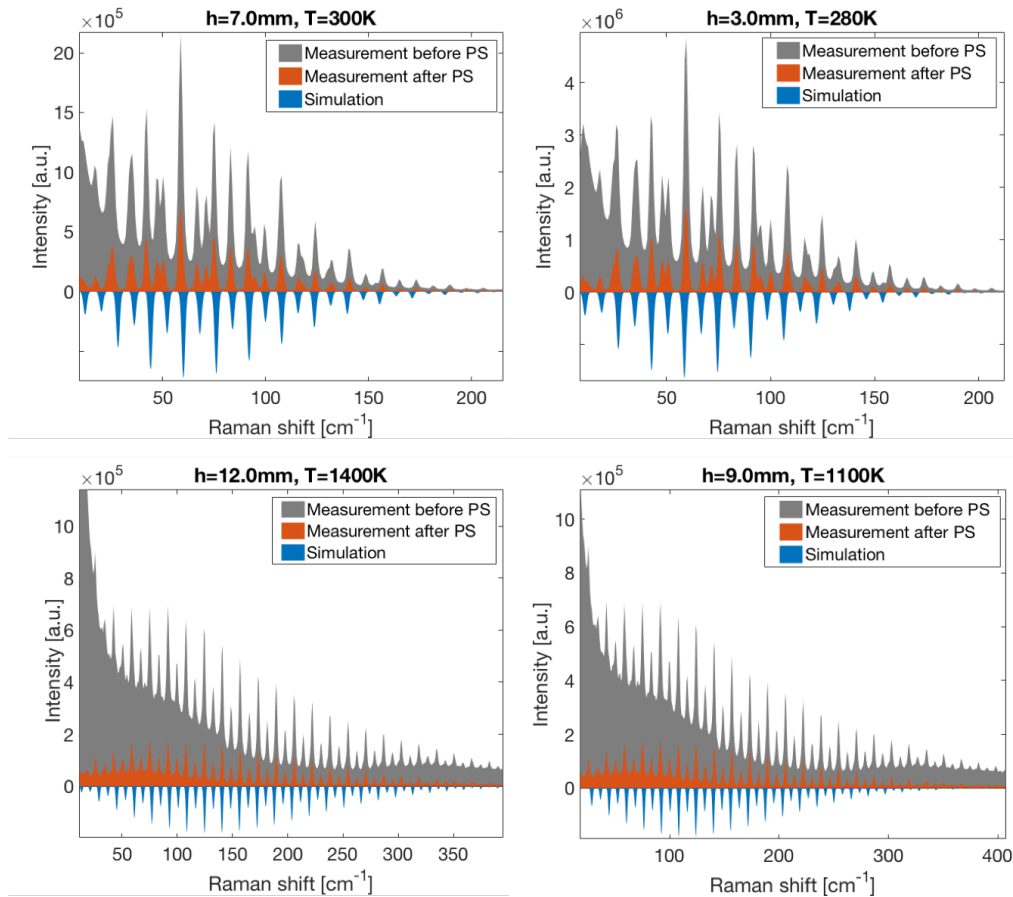


Figure 23: Measured Raman spectra before and after PS process and the corresponding simulated spectra at the four different heights in the methane/air flame. Amplitude of the simulated spectra is adapted to the PS spectra and reflected on the Raman shift axis to clarify. The temperature values are obtained from the simulations.

4 Experimental Method and Results for the DMD-PS spectrometer

4.1 Digital Micro-mirror Device (DMD)

A DMD is a device that contains an array of individual micro-mirrors in micrometer size. These micro-mirrors can be flipped to a small angle (12 degrees), either positive or negative. The DMD can work as a spatial light modulator and modulate the light both in spatial and time domain depending on the system needed. The DMD used in the experiment is model V-9500 DLP 0.95 1080p, consisting of micrometer sized ($10.8 \times 10.8 \mu\text{m}^2$) micro-mirrors in a 1920×1080 array and a total active mirror array area of $20 \times 11.7 \text{ mm}^2$. The usable spectral range covers wavelengths from 350 nm to 2500 nm. A LabVIEW program is used to control the DMD and couple it with the detector.

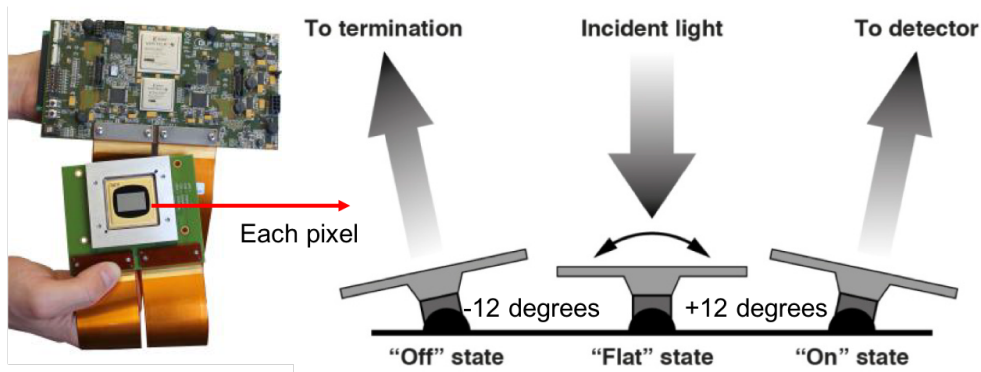


Figure 24: Photograph of the DMD and illustration the basic mechanical principle [24]. Each DMD pixel can be flipped to ON or OFF state with a high refreshing rate.

Each DMD pixel is an electro-mechanical element comprised of a mirror which is attached to a torsional hinge and a hidden yoke along the diagonal direction. Such mechanics allow each pixel to flip individually to either +12 degrees (ON state) or -12 degrees (OFF state). By convention, the ON state usually refers to the state where the reflection path of the light is placed towards the detector. The OFF state accordingly refers to the state where the reflection path is tilted away from the detector. Image information can be loaded to the DMD through the controller board circuit via 12-inch flex cables. Gray scale information can be used as input to set the percentage of time spent in each state.

4.2 The Optical design for the DMD-PS spectrometer

For building the novel spectrometer, a Czerny-Turner spectrometer configuration was selected as it has a number of benefits, such as experimental simplicity and 2D capability. The arrangement is shown in figure 25. The PS method was employed by installing a transmission Ronchi grating onto the entrance slit. The DMD was situated after the second concave mirror, where the detector is usually located in a conventional design. The

spectral image was focused onto the DMD surface and then in the ON state light was reflected towards the detector. After collected and focused by the camera lens, the signal image was detected by a CCD camera.

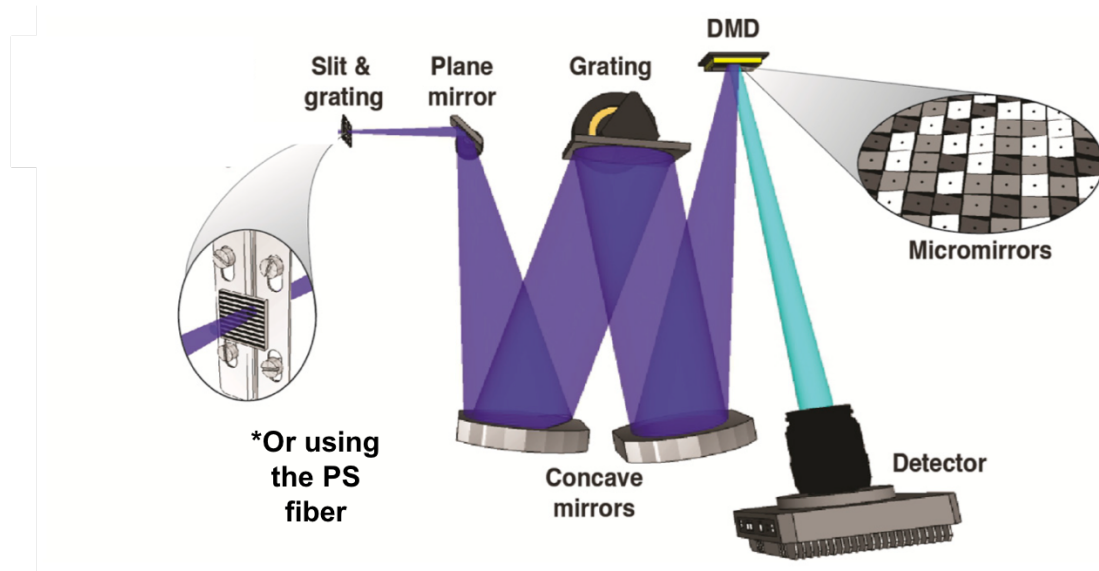


Figure 25: Schematic figure of the optical design for the novel DMD-PS spectrometer. Image from [9].

4.2.1 Ray tracing simulation

The Czerny-Turner spectrometer configuration was simulated in using the software FRED [25] (Photon Engineering LLC), as shown in figure 26. The diffraction grating has a groove frequency of 300 l/mm and the focal length of the two concave mirrors is 762 mm. Considering the DMD pixel size, the estimated best spectral resolution at the focal plane in the simulation (where the DMD is placed) is 0.4 nm.

4.2.2 Alignment of the spectrometer

The spectrometer was aligned according to the design in figure 25 and the implemented alignment is displayed in figure 27. The system was placed on a movable optical table so that it is possible to install it in other setups for further investigation. The signal light was focused onto the slit tagged with the transmission Ronchi grating. The slit width was controlled manually with a range from 50 μm to 5 mm. The light was then reflected by the plane mirror to the first concave mirror (focal length 762 mm). The first concave mirror collimated and reflected the light onto the diffraction grating (groove density 300 l/mm). The monochromatic light was collected by the second concave mirror (focal length 762 mm) and focused onto the DMD. By placing the DMD mirror at a specific angle, the ON state light can be collected by the detector.

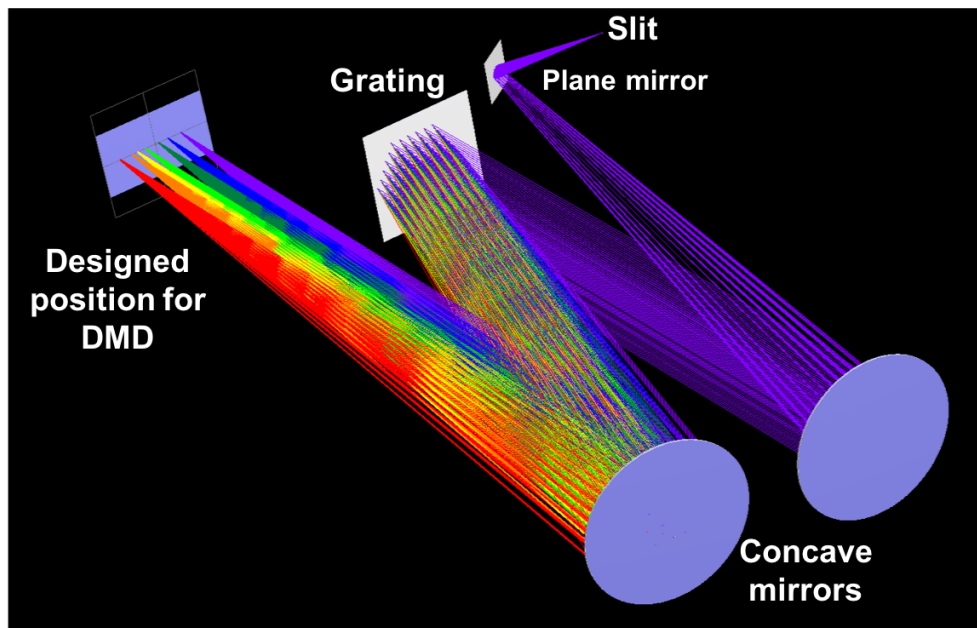


Figure 26: The ray tracing simulation of the Czerny-Turner spectrometer in FRED.

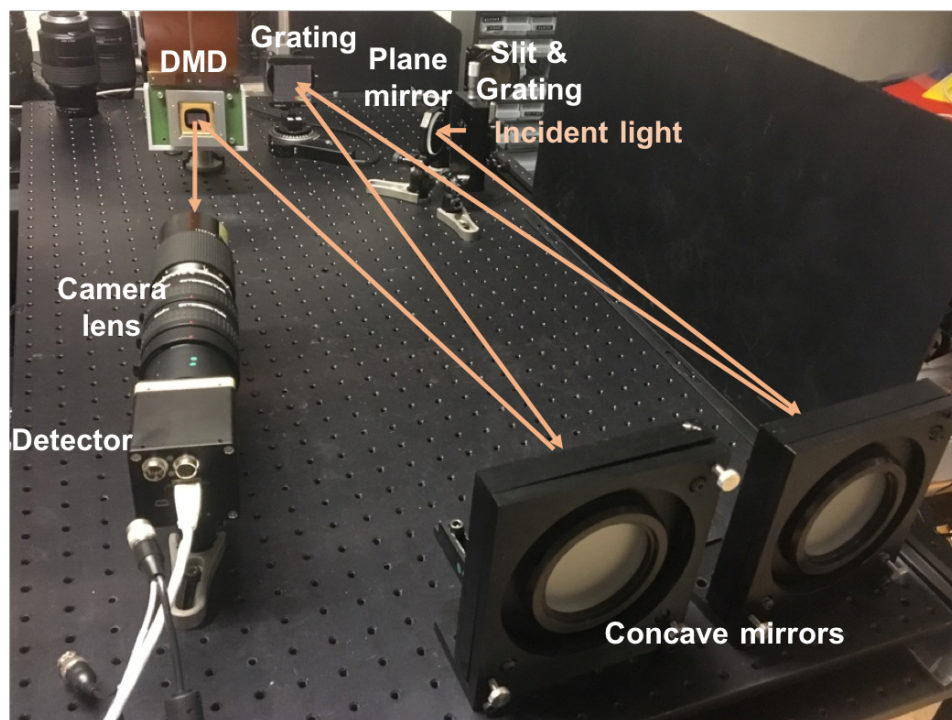


Figure 27: Photograph of the DMD-PS spectrometer. The system is placed on a movable optical table.

Note that it is crucial to keep the light path in the same horizontal plane, i.e. to ensure that the spectral lines on the detector plane is at the same height above the optical table. Practically, a Continuous Wave (CW) laser is useful to check if all the diffraction orders are on the same height, as shown in figure 28 a). One of the experimental challenges here arises from the special rotation angle (± 12 degrees along the diagonal) of the DMD. This means that if the DMD is positioned vertically to the light path plane, the ON state reflection will be 12 degrees upwards and 45 degrees leftwards, making it challenging to place the detector. To solve this issue, the DMD was mounted onto an adjustable level plate and was rotated to a specific angle (shown in 28 b)) so that the ON state reflection can be parallel to the light path plane. In this way the detector can be normally placed on the optical table without the need for a custom-made holder to match with the DMD. However, this solution makes the areas on the edges of the DMD fall outside of the focal plane of the collecting concave mirror, which means that part of the spatial resolution on the upper and lower edges is reduced. In practice, it was partly compensated for by using a camera lens with a large depth of field.

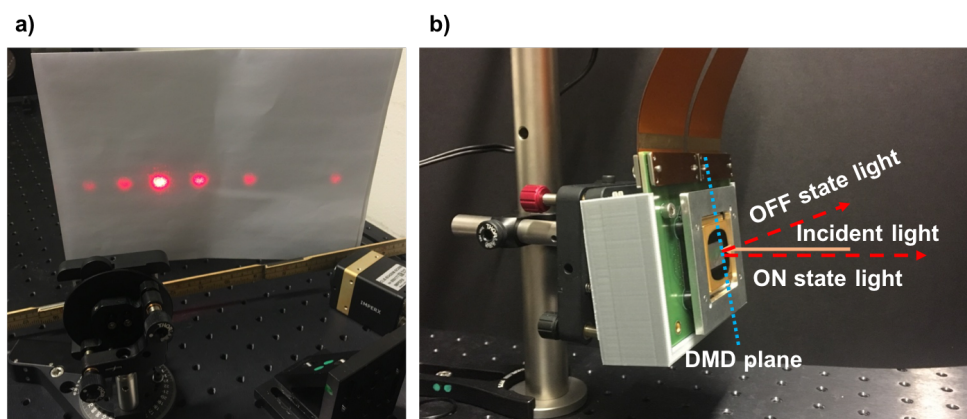


Figure 28: a) The diffraction orders reflected by the grating while aligning. b) The DMD is mounted on a level plate and adjusted to an angle where the ON state reflection is parallel with the incident light (horizontally).

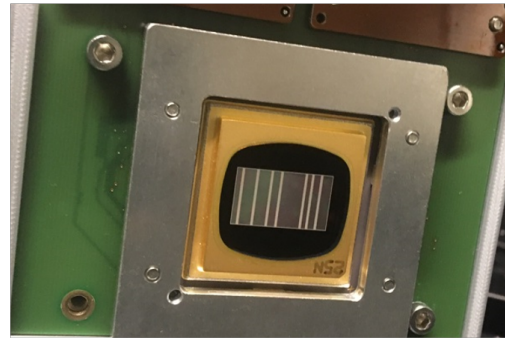
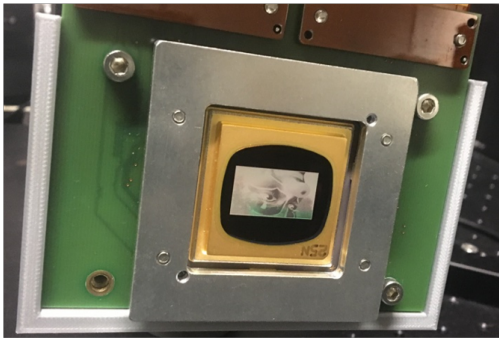
4.3 Results

Several measurements were performed in order to verify the performance of the novel DMD-PS spectrometer, including test image transfer performance, spectral resolution and peak removal ability.

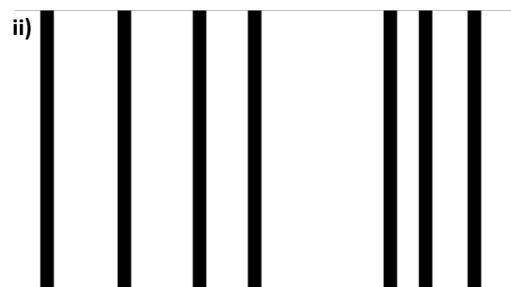
4.3.1 Image transfer performance

The image quality on the detector is greatly dependent on if the incident light is correctly focused onto the DMD plane and if the DMD image is properly transferred to the CCD.

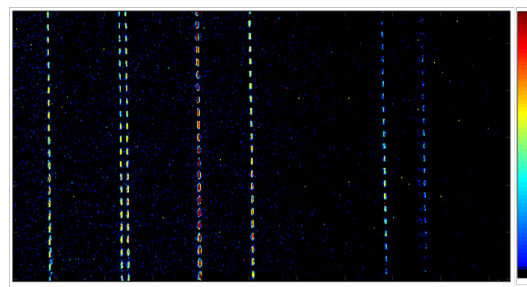
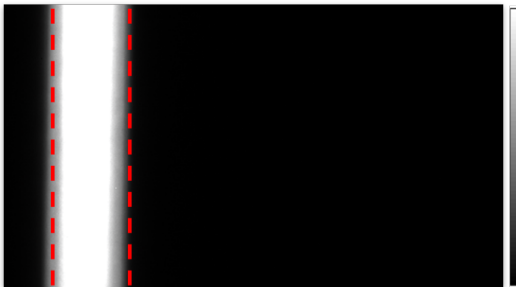
a) The DMD loaded with images (vertical flip)



b) The loaded images i) and ii)



c) The detected spectrum images when the DMD is loaded with a full-ON image



d) The detected spectrum images when the DMD is loaded with the images i) and ii)

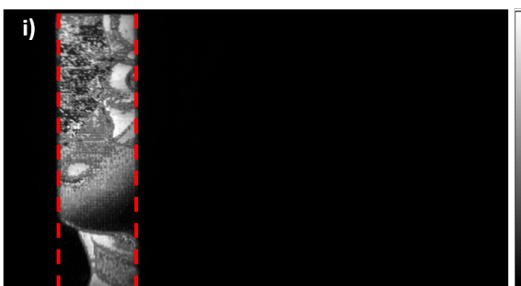


Figure 29: a) The photos of the DMD loaded with images. Note that the display is vertically flipped. b) The loaded images. i) is a grey-scale picture and ii) is a black and white picture. c) The detected spectrum images when the DMD is loaded with a blank (white) image with two different light sources. d) The detected spectrum images when the DMD is loaded with the image i) and ii) with the corresponding light sources above.

As shown in figure 29 , two images are displayed on the DMD and ready to be transferred. The left figure i) is a 16-bit grey-scale clown picture. The right figure ii) is a black and white picture acting as a mask where the black lines are intended to block the spectral lines from an argon emission lamp. Figure 29 c) shows the detected spectrum images when a blank picture (DMD with full-ON state) is loaded with two different light sources. Figure 29 d) shows the detected spectrum images when pictures i) and ii) are loaded with the two light sources respectively. As for the clown image, the region highlighted by red dotted lines is where the spectral line of the light source overlaps with the picture. The clown image is transferred and the details are well retained. As for the black and white image, the spectral lines from the argon emission lamp are totally rejected by the black lines where the DMD pixels are triggered OFF state, which also indicates the image is successfully transferred to the detector.

4.3.2 Spectral resolution

The spectral resolution was approximately estimated by looking at the sodium double lines (589.0 nm and 589.6 nm) as shown in figure 30. The entrance slit was closed down as much as possible to about 50 μm to achieve the smallest FWHM of the spectral peak. The estimated best spectral resolution of the spectrometer was about 0.3 nm, which matches with the prediction of 0.4 nm in the FRED simulation.

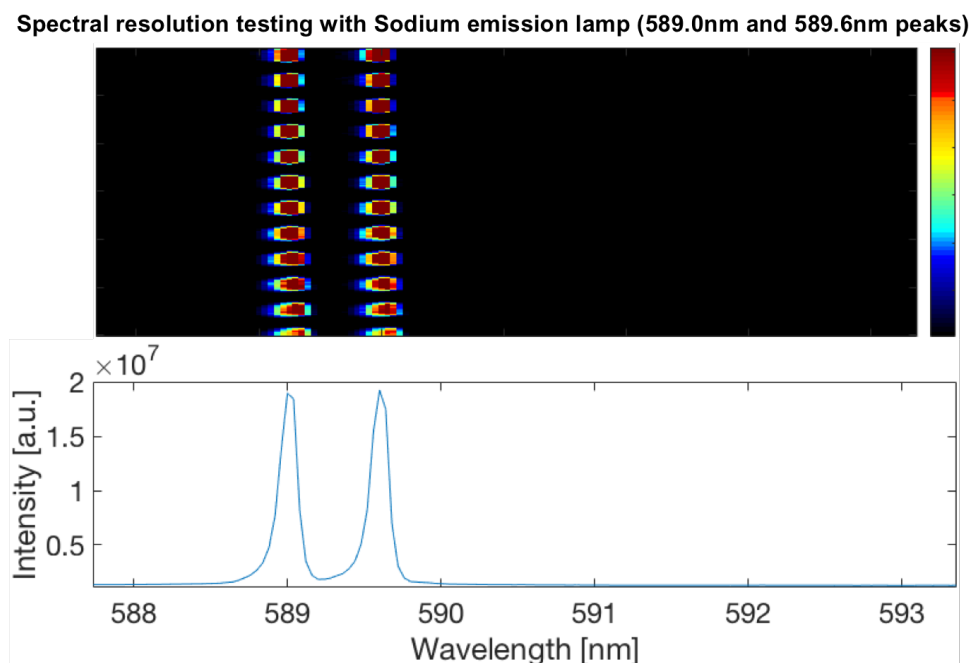


Figure 30: The PS spectrum of the sodium double lines at wavelengths 589.0 nm and 589.6 nm to estimate the spectral resolution.

4.3.3 Single peak removal

One of the major goals of implementing the DMD in the spectrometer is to be able to block any spectral peak and therefore improve the dynamic range. A black blockage rejects any incident light of that area to transfer into the detector. A reasonable concern about this process is that if the spectrum will be interfered by introducing the DMD blockage, since the spectral region where is blocked by the DMD will have different background level comparing to the other regions.

Masks of one blockage (black line) with several widths (20, 40, 50, 60 and 80 DMD pixels) were created and loaded on the DMD. Figure 31 shows the resulting PS spectra when different masks are applied. Note that the intensity is in logarithm scale. The spectrum is from an argon emission lamp. Note that the blue line is the spectrum when a blank image is applied. In the zoomed in view on the left, comparing the orange line with the blockage width of 20 DMD pixels with the other lines with larger blockage width, it indicates that the spectral line of the local slit width is about 30-40 DMD pixel-size. Moreover, as shown in the both zoomed in views, the other areas of the spectrum is not affected by the DMD rejection. It is because of the PS process, for the background level is effectively reduced and remains the same level as that of the other regions.

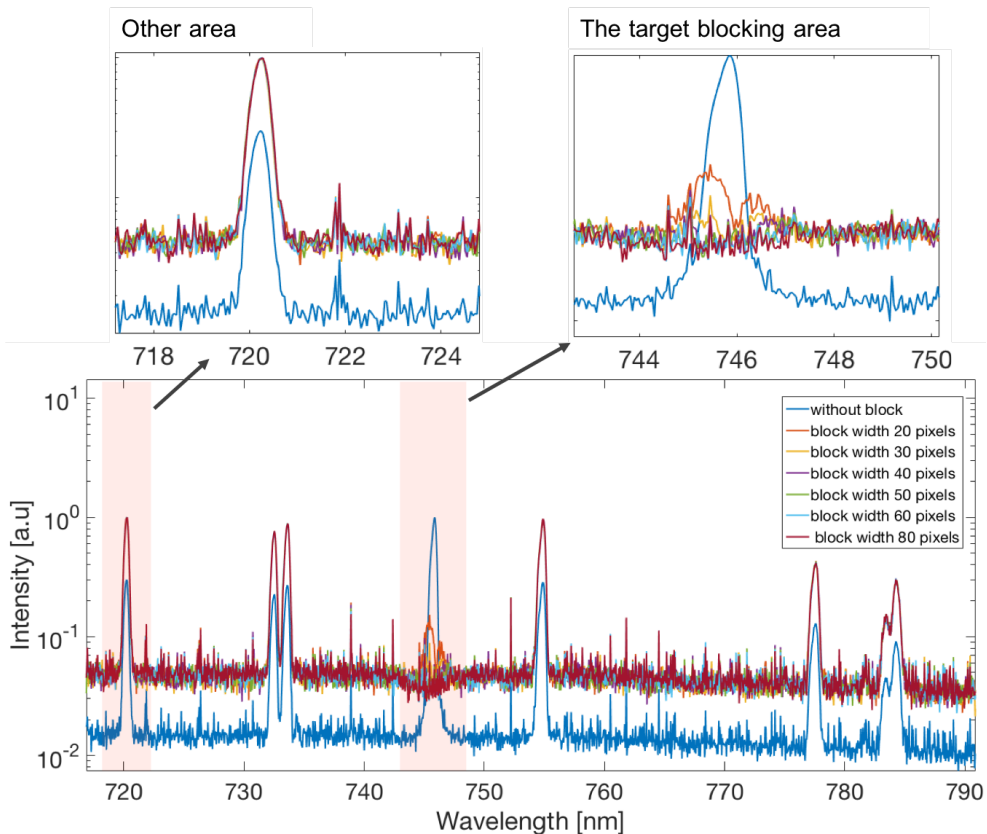


Figure 31: The PS spectra of an argon emission lamp when single-peak blocking masks with different DMD blockage width are applied. The intensity is in logarithm scale.

4.3.4 Multiple peaks removal

In this measurement, a mask covering all the spectral peaks in the range was created and applied. As indicated in the comparison of the spectra before and after PS process in figure 32, the background level is effectively reduced by PS. The resulting spectrum has almost a background level close to 0. This shows the possibility to improve the dynamic range by blocking the strong peak(s) with DMD and increase the accumulation time on the detector. The estimated improvement in dynamic range was a factor of at least 50 over the conventional way.

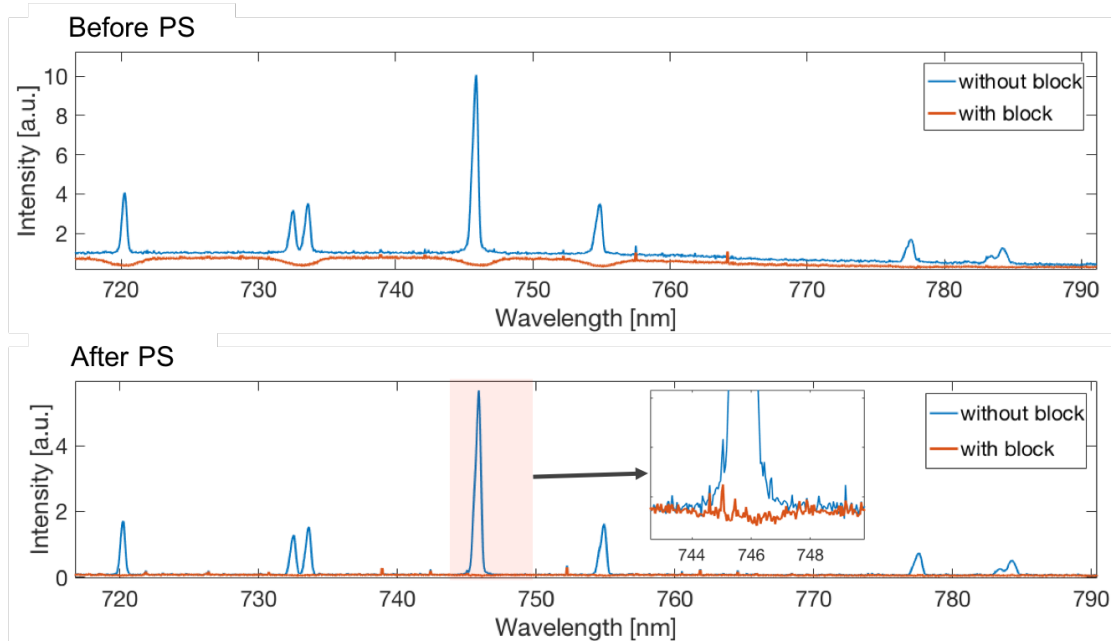


Figure 32: The spectra before PS and after PS process of an argon emission lamp when all peaks are blocked by a DMD mask.

5 Experimental Method for Thomson measurements in plasma

5.1 Setup

Figure 33 shows the experimental setup of the Thomson scattering measurements. Due to the fact that the plasma channel size is smaller than the probe volume of the multi-pass pattern, the set up was changed into a double-pass arrangement to create a smaller probe volume. In addition, the Ronchi grating was used for PS modulation since more light can be collected with this configuration.

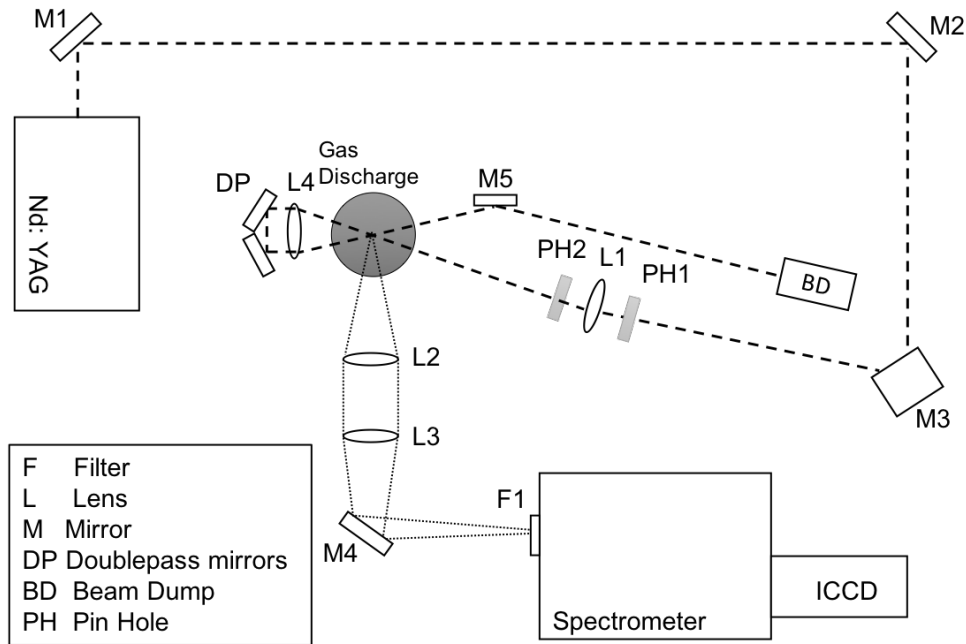


Figure 33: Schematic illustration of the experimental setup for Thomson scattering measurements using the Ronchi grating for PS modulation.

5.2 Plasma Measurements

The plasma was generated in a gas discharge setup, as shown in figure 34.

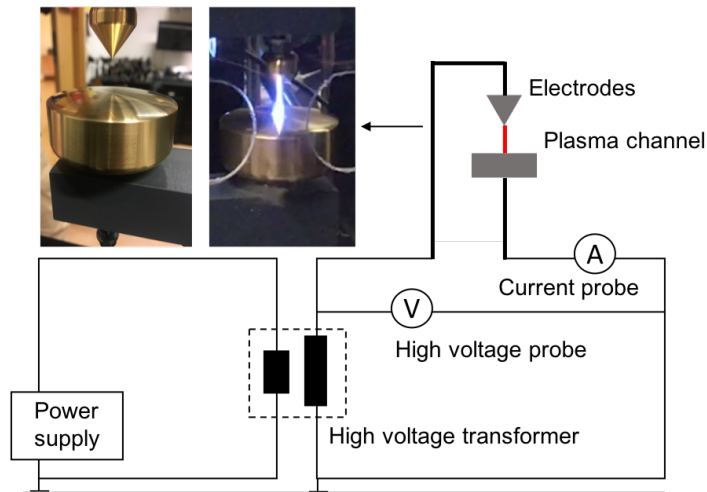


Figure 34: Schematic illustration and photo of the gas discharge plasma setup.

The AC power supply of the discharge system was operated at 40 kHz, corresponding to a period of $12.5 \mu\text{m}$. A burst mode at a 100 Hz repetition rate of the power supply

is used in order to facilitate the synchronization of the laser and detection system with the plasma generation [26]. Laser-induced Thomson scattering was synchronized with the plasma generation and the camera gating by using a signal generator. However, the synchronization process was highly disturbed by the electromagnetic field created by the strong current of the plasma. Therefore, shielding is crucial for the measurements. Another experimental challenge is to match the laser probing with the plasma channel, meaning it is important to generate a stable plasma.

5.3 Preparation measurement

Before starting the Thomson scattering measurements, it is necessary to confirm that the spectral resolution of the system is high enough to detect the slight Doppler broadening effect from the plasma [27]. The plasma energy of the gas discharge that is used in the experiment is about 0.5 eV. The spectral broadening is calculated to be on the order of about 0.5 nm, i.e. 30 cm^{-1} Raman shift. Here, a pure nitrogen flow in room temperature was used to verify the detection limit in wavenumber. The long-pass filter was adjusted to an angle in order to have lowest cut-off wavelength. As shown in figure 35, combined with the PS method, the system is able to resolve the spectrum down to 10 cm^{-1} from the laser line with a resolution under 10 cm^{-1} . This means that it is possible to investigate the laser-induced Thomson scattering in such an experimental setup.

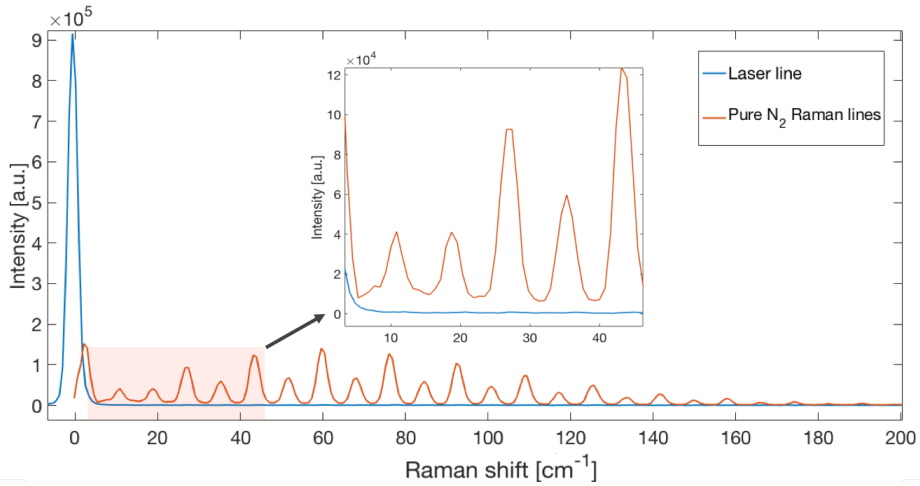


Figure 35: Comparison between rotational PS Raman spectrum of pure nitrogen flow in room temperature and laser line to verify the detection limit of the experimental setup in wavenumber.

6 Quantifying the imaging quality of PS

Signal-to-Noise Ratio (SNR)

The Signal-to-Noise Ratio is defined as the ratio of the power level of the signal to the power level of the background noise [28]. One way of improving the SNR in digital cameras is pixel binning by combining the electric charge of the adjacent CCD chip pixels into a super pixel (usually along the spatial direction because binning on the wavelength direction decreases the spectral resolution). By doing this, the relative sensitivity can be increased by the factor of the binning pixel number. For one-dimensional spectroscopic measurements, it is common to bin all the pixels along the spatial direction into one column. However, PS requires 2D acquisition, which eliminates the possibility of full range binning, yet partial binning, e.g. 4×1 binning is applicable.

Modulation Contrast Test

The comparison between the contrast of an image and that of the original object can be used to describe the imaging performance of the optical system [19, 29, 30]. Usually, the concept of Modulation transfer Function (MTF), which determines how much of the contrast in the original object is maintained in the image as a function of spatial frequency, is used to quantify the performance of the imaging system [31]. The contrast of an image can be calculated as

$$\text{Contrast} = \frac{I_{max} - I_{min}}{I_{max} + I_{min}} \quad (6.20)$$

where I_{max} is the maximum intensity and I_{min} is the minimum intensity. Here, similarly to MTF, the relative contrast is defined as the ratio of the resulting imaging contrast to the object contrast as a function of binned pixel number .

The PS method creates a modulation pattern of a single frequency. While using the Ronchi grating as the object, the striped pattern of black and white line-pairs is imaged onto the detector through the spectrometer. In an ideal case, the contrast of the resulting image is 1 and the object contrast is also 1. The relative contrast can be obtained by comparing the contrast of the image and that of the object directly. Alternatively, the relative contrast can be calculated by using the Fourier transform and compare the amplitudes of the zeroth order to that of the first order of the periodic PS modulation. In this case, by using the amplitude of the first order frequency a'_f and that of the zeroth component a_0 , the relative contrast C can be deduced as [32]

$$C = \left| \frac{\pi a'_f}{2a_0} \right| \quad (6.21)$$

As for PS method, the zeroth order (DC component) and the first order switch positions after processing, as explained in section 2.3 and shown in figure 36. The data is normalized to the zeroth order.

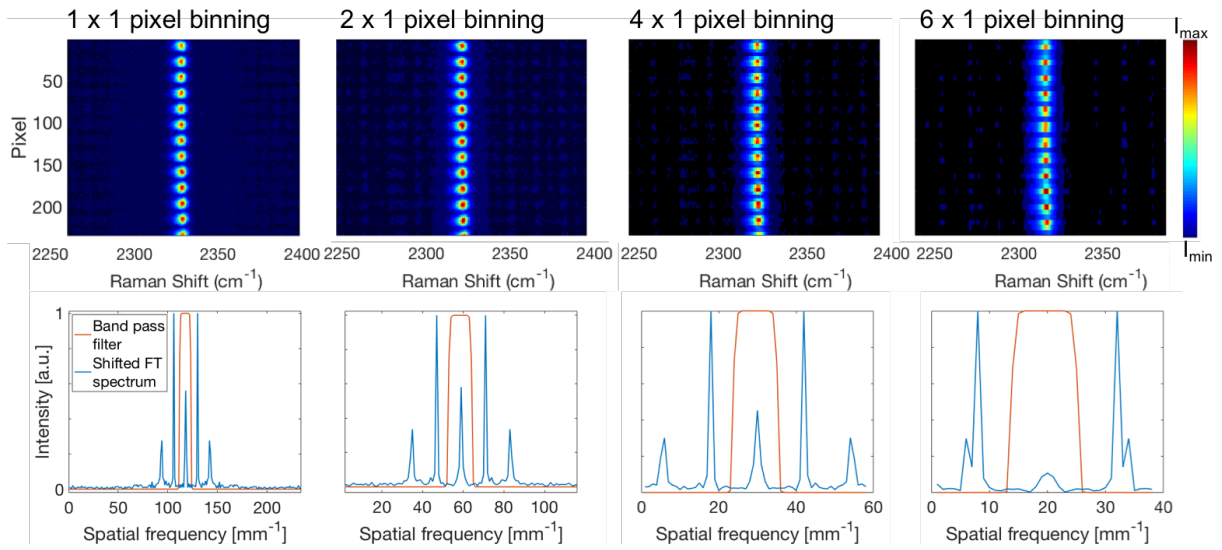


Figure 36: The 2D spectral images using the PS fiber in different pixel binning conditions of nitrogen vibrational peak in room temperature air. The corresponding shifted FT spectra is shown in the second row of the figure, where the zeroth order (DC component) and the first order switch positions.

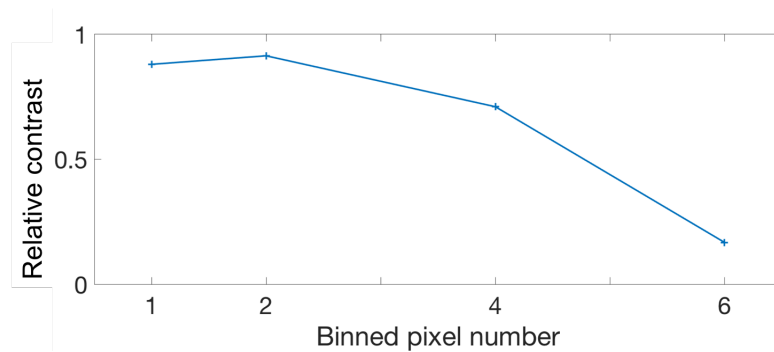


Figure 37: The relative contrast of PS imaging vs the binned pixel number calculated from the experiment using the PS fiber.

Figure 36 shows the unprocessed 2D PS spectra using the PS fiber of N₂ vibrational Raman peak in room temperature air for different pixel binning numbers and their shifted FT spectra with the band pass filters. Figure 36 illustrates that there is an overall decreasing trend of the modulation frequency as the pixel binning number increases. The reason is likely that with increase of the pixel binning number, the intensity of the pixels on the edge of the PS pattern is averaged and therefore destroys the clearness of the pattern. While the PS process strongly relies on the the pattern, the blurred pattern will affect the performance of PS. This issue can be avoided if the size of the binned pixel can match with the periodicity of the Ronchi pattern. Figure 37 indicates the relative contrast decreases

as the pixel number increases. This may arise from the decreasing sampling with binning.

7 Conclusion

In this thesis, several methods for spectroscopic detection improvement were developed and implemented in a high-performance laser system to investigate Raman- and Thomson scattering spectroscopy in combustion and plasma. With these methods, it is possible to obtain cleaner spectra by suppressing stray light and enhancing dynamic range in the spectral area close to strong lines in laser spectroscopy.

The stray-light suppression method PS has been presented and demonstrated in Raman measurements. It is shown that the background level can be efficiently reduced by a factor of 10 or more. Such a method emphasizes the smaller peaks in the spectrum so that minor species can be detected, for example the hydrocarbons in combustion. Moreover, the improved spectral quality allow for more accurate temperature evaluation. Nevertheless, a new approach with a customized fiber, capable of stray-light rejection with the PS algorithm is verified and experimentally demonstrated. The fiber approach has several advantages including improving the flexibility in the detection system. In measurements with limited optical access, the introduction of a fiber allows for convenience and flexibility. Especially in a vessel where both limited access and stray light issues arise. The DMD-PS method for high dynamic range combined with stray light suppression imaging has been investigated and implemented in a spectrometer. It is shown that the dynamic range can be improved by a ratio of at least 50 compared to conventional imaging method. The usage of the DMD allows for high dynamic range imaging without damaging the CCD chip. Also, multiple peaks removal can be achieved by applying masks with multiple blockage onto the DMD. The DMD-PS spectrometer has the potential to be applied to spectroscopic measurements such as Raman and Thomson- scattering measurements.

The experimental setup implemented with the PS method, using both Ronchi grating and the PS fiber approach, was tested for Raman spectroscopy in combustion. Laminar premixed hydrocarbon gas/air flames were characterized in species by using the setup. Concentration and temperature evaluation were performed and it shows good agreement with the theoretical simulations. Initial tests were made to perform Raman- and Thomson scattering in discharge plasma.

8 Outlook

Further development of the PS and DMD-PS methods would benefit for future work in Raman- and Thomson scattering spectroscopy. The PS fiber would benefit from a better design since the light loss issue of the present design limits the detection sensitivity. The size of the fiber bundle is larger than the entrance slit width of the spectrometer resulting in light loss which could be optimized. Reducing the fiber size would also give a higher modulation frequency and improve the PS filtering efficiency. There is a technical issue

with the detector used for the present DMD-PS spectrometer that restricts the acquisition time. A detector with longer acquisition time would allow for more precise estimation on the dynamic range improvement. The DMD in the present DMD-PS spectrometer configuration is tilted vertically in order to compensate for the operating angle of 12 degrees. This leads to a slight disagreement between the focal plane of the concave mirror and the DMD causing defocus at the detector. It would be beneficial to design and manufacture a stand for the detector to face towards the DMD without tilting the DMD. In addition, the Schimepflug principle could be implemented to compensate for this shortcoming. In the future work, the improved DMD-PS spectrometer would be beneficial to use in different spectroscopic measurements.

As mentioned in section 3.4, the combined spectral lines needs for careful analysis to obtain accurate concentration evaluation, such as H_2O and CO . Fitting of the individual lines can improve the accuracy of such species. In the temperature evaluation, the measured spectra show an offset in wavelength compared to the simulations meaning that more accurate wavelength calibration of the spectrometer is needed. As for the Thomson scattering measurements, the current task is to achieve laser-plasma-camera synchronization to ensure the observed signal is from the plasma. Also, it is a challenging task to distinguish the Thomson scattering signal from the electrons from the Raman scattering signals from air.

9 Acknowledgement

First and foremost, I would like to thank my supervisors Andreas Ehn, Christian Brackmann and Elias Kristensson for giving me this opportunity to work on this fascinating project and all their support during this time. I also want to thank Haisol Kim, Jim Larsson, Torsten Methling, Chengdong Kong and Henrik Johansson for all the help throughout the project. In addition, I want to thank all the people at the Division of Combustion Physics for providing a lovely and warm working environment. A special thanks goes to my parents and my boyfriend Rickard Lydahl who have been supporting me all the time.

References

- [1] Wolfgang Demtröder. *Laser spectroscopy: basic concepts and instrumentation*. Springer Science & Business Media, 2013.
- [2] Alan C Eckbreth. *Laser diagnostics for combustion temperature and species*, volume 3. CRC Press, 1996.
- [3] Colin N Banwell, Elaine M McCash, et al. *Fundamentals of molecular spectroscopy*, volume 851. McGraw-Hill New York, 1994.
- [4] Ewen Smith and Geoffrey Dent. *Modern Raman spectroscopy: a practical approach*. John Wiley & Sons, 2013.
- [5] Wonchul Lee. *Development of Raman and Thomson scattering diagnostics for study of energy transfer in nonequilibrium, molecular plasmas*. PhD thesis, The Ohio State University, 2003.
- [6] R Donaldson. Stray light in monochromators. *Journal of Scientific Instruments*, 29(5):150, 1952.
- [7] Richard E Poulson. Test methods in spectrophotometry: Stray-light determination. *Applied Optics*, 3(1):99–104, 1964.
- [8] Elias Kristensson, Joakim Bood, Marcus Alden, Emil Nordström, Jiajian Zhu, Sven Huldt, Per-Erik Bengtsson, Hampus Nilsson, Edouard Berrocal, and Andreas Ehn. Stray light suppression in spectroscopy using periodic shadowing. *Opt. Express*, 22(7):7711–7721, Apr 2014.
- [9] Elias Kristensson, Andreas Ehn, and Edouard Berrocal. High dynamic spectroscopy using a digital micromirror device and periodic shadowing. *Optics Express*, 25(1):212–222, 2017.
- [10] Miaoxin Gong. Fiber-based stray light suppression in spectrometers, 2017. Student Paper.
- [11] Marcus Aldén. *Applications of laser techniques for combustion studies*. PhD thesis, Lunds universitet, 1983.
- [12] Ian H Hutchinson. Principles of plasma diagnostics. *Plasma Physics and Controlled Fusion*, 44(12):2603, 2002.
- [13] S. H. Glenzer, W. Rozmus, B. J. MacGowan, K. G. Estabrook, J. D. De Groot, G. B. Zimmerman, H. A. Baldis, J. A. Harte, R. W. Lee, E. A. Williams, and B. G. Wilson. Thomson scattering from high- Z laser-produced plasmas. *Phys. Rev. Lett.*, 82:97–100, Jan 1999.

- [14] M. A. A. Neil, R. Juškaitis, and T. Wilson. Method of obtaining optical sectioning by using structured light in a conventional microscope. *Opt. Lett.*, 22(24):1905–1907, Dec 1997.
- [15] S Mann and R Picard. Being 'undigital' with digital cameras. *MIT Media Lab Perceptual*, 1:2, 1994.
- [16] Paul E Debevec and Jitendra Malik. Recovering high dynamic range radiance maps from photographs. In *ACM SIGGRAPH 2008 classes*, page 31. ACM, 2008.
- [17] Erik Reinhard, Wolfgang Heidrich, Paul Debevec, Sumanta Pattanaik, Greg Ward, and Karol Myszkowski. *High dynamic range imaging: acquisition, display, and image-based lighting*. Morgan Kaufmann, 2010.
- [18] Davide Giassi, Bolun Liu, and Marshall B Long. Use of high dynamic range imaging for quantitative combustion diagnostics. *Applied optics*, 54(14):4580–4588, 2015.
- [19] Elias Kristensson and Andreas Ehn. Improved spectral sensitivity by combining periodic shadowing and high dynamic range imaging. *Spectroscopy Letters*, 49(2):91–95, 2016.
- [20] Henrik Johansson. Development of optimized raman spectroscopy setup for species detection in flames, 2016. Student Paper.
- [21] David G Goodwin, Harry K Moffat, and Raymond L Speth. *Cantera: An object-oriented software toolkit for chemical kinetics, thermodynamics, and transport processes*. Caltech, Pasadena, CA, 2009.
- [22] Peter Glarborg, James A Miller, Branko Ruscic, and Stephen J Klippenstein. Modeling nitrogen chemistry in combustion. *Progress in Energy and Combustion Science*, 67:31–68, 2018.
- [23] C. M. Western. Pgoopher, a program for simulating rotational, vibrational and electronic spectra. *Journal of Quantitative Spectroscopy and Radiative Transfer*, 186(1):221–242, 2016.
- [24] Benjamin Lee. Introduction to 12 degree orthogonal digital micromirror devices (dmds). *Texas Instruments*, DLPA008B–July 2008–Revised February 2018.
- [25] Richard N. Pfisterer James E. Harvey, Ryan G. Irvin. Modeling physical optics phenomena by complex ray tracing. *Optical Engineering*, 54(3):1 – 12 – 12, 2015.
- [26] Z.W. Sun, J. J. Zhu, Z.S. Li, M. Aldén, F. Leipold, M. Salewski, and Y. Kusano. Optical diagnostics of a gliding arc. *Opt. Express*, 21(5):6028–6044, Mar 2013.
- [27] Benjamin Vincent, Sedina Tsikata, Stéphane Mazouffre, Tiberiu Minea, and Jérôme Fils. A compact new incoherent thomson scattering diagnostic for low-temperature plasma studies. *Plasma Sources Science and Technology*, 27(5):055002, may 2018.

- [28] A Bruce Carlson. Communication systems: An introduction to signals and noise in electrical communication/a. bruce carlson.
- [29] David L Sedarsky, Edouard Berrocal, and Mark A. Linne. Quantitative image contrast enhancement in time-gated transillumination of scattering media. *Optics express*, 19 3:1866–83, 2011.
- [30] Tzu Cheng Chao, Hsiao-Wen Chung, W. Scott Hoge, and Bruno Madore. A 2d mtf approach to evaluate and guide dynamic imaging developments. *Magnetic resonance in medicine*, 63 2:407–18, 2010.
- [31] E. Hecht. *Optics, Global Edition, Fifth Edition*. Pearson Education, Harlow, England, 2017.
- [32] Edouard Berrocal, Sven-Göran Pettersson, and Elias Kristensson. High-contrast imaging through scattering media using structured illumination and fourier filtering. *Opt. Lett.*, 41(23):5612–5615, Dec 2016.